Redox Biology 85 (2025) 103736

Contents lists available at ScienceDirect

Redox Biology

journal homepage: www.elsevier.com/locate/redox

Translocation of SIRT6 promotes glycolysis reprogramming to exacerbate diabetic angiopathy

Kemiao Pang [a], Jiayi Huang [a], Shiwu Zhang [a], Yinghui Guan [b], Ning Zou [c], Jiaxin Kang [a], Haining Du [a], Dechao Zhao [d], Denis V. Abramochkin [e], Heyu Chen [a], Nan Zhang [f], Yunyan Gu [f], Ning Liu [a], Yining Niu [a], Ziqi Xiong [a], Xueya Zhang [a], Fanghao Lu [a], Huitao Fan [g,h,i,*****], Jinwei Tian [a,j,****], Bo Yu [a,k,***], Shuijie Li [k,l,m,**], Weihua Zhang [a,j,*]

[a] Department of Cardiology, Department of Pathophysiology, Key Laboratory of Myocardial Ischemia, Ministry of Education, Second Affiliated Hospital of Harbin Medical University, China
[b] Department of Vascular Surgery, First Affiliated Hospital of Harbin Medical University, China
[c] Center for Endemic Disease Control, Chinese Center for Disease Control and Prevention, Harbin Medical University, China
[d] Department of Cardiology, First Affiliated Hospital of Harbin Medical University, China
[e] Department of Human and Animal Physiology, Biological Faculty, Lomonosov Moscow State University, Russia
[f] College of Bioinformatics Science and Technology, Harbin Medical University, China
[g] NHC Key Laboratory of Cell Transplantation, The First Affiliated Hospital of Harbin Medical University, China
[h] Department of Critical Care Medicine, The First Affiliated Hospital of Harbin Medical University, China
[i] Department of Hematology, The First Affiliated Hospital of Harbin Medical University, China
[j] Heilongjiang Provincial Key Laboratory of Panvascular Disease, China
[k] State Key Laboratory of Frigid Zone Cardiovascular Diseases (SKLFZCD), China
[l] Department of Biopharmaceutical Sciences, College of Pharmacy, Harbin Medical University, China
[m] Heilongjiang Province Key Laboratory of Research on Molecular Targeted Antitumor Drugs, China

ARTICLE INFO

Keywords:
Type 2 diabetes (T2D)
Cell proliferation
Sirtuin 6 (SIRT6)
Hydrogen sulfide (H_2S)
Glycolysis

ABSTRACT

Diabetic angiopathy, a major complication of type 2 diabetes mellitus (T2DM), is driven by vascular dysfunction, metabolic reprogramming, and oxidative stress. NAD^+-dependent deacetylase SIRT6, located in the nucleus, is recognized for its role in modulating cardiovascular and metabolic homeostasis through histone deacetylation. However, the functions and mechanisms of accumulation of cytoplasmic SIRT6 in T2DM remain to be elucidated. Herein, a previously unrecognized cytoplasmic role for SIRT6 is identified in promoting pathological glycolysis during diabetic vascular remodeling. Vascular smooth muscle cell (VSMC) proliferation is observed, which is correlated with protein deacetylation, especially SIRT6, which translocated to the cytoplasm mediated by Importin 13 (IPO13). Furthermore, the accumulation of cytoplasmic SIRT6 facilitates its interaction with enolase 3 (ENO3), a newly discovered downstream target. This interaction promotes ENO3 deacetylation, enhances downstream phosphoenolpyruvic acid (PEP) levels, and thereby drives glycolysis reprogramming, ultimately leading to the pathological changes associated with diabetic angiopathy. Notably, exogenous hydrogen sulfide (H_2S) restores S-sulfhydration of SIRT6 at cysteine 141, counteracting the SIRT6-ENO3 interaction, suppressing glycolysis, and mitigating VSMC hyperproliferation. This study provides novel insights into the SIRT6-ENO3

* Corresponding authors. Department of Cardiology, Department of Pathophysiology, Key Laboratory of Myocardial Ischemia, Ministry of Education, Second Affiliated Hospital of Harbin Medical University, China.
** Corresponding authors. State Key Laboratory of Frigid Zone Cardiovascular Diseases (SKLFZCD), China.
*** Corresponding authors. State Key Laboratory of Frigid Zone Cardiovascular Diseases (SKLFZCD), China.
**** Corresponding author. Department of Cardiology, Department of Pathophysiology, Key Laboratory of Myocardial Ischemia, Ministry of Education, Second Affiliated Hospital of Harbin Medical University, China.
***** Corresponding author. Department of Hematology, The First Affiliated Hospital of Harbin Medical University, China.
E-mail addresses: huitaofan@hrbmu.edu.cn (H. Fan), tianjinwei@hrbmu.edu.cn (J. Tian), yubo@hrbmu.edu.cn (B. Yu), shuijie.li@hrbmu.edu.cn (S. Li), zhangweihua@hrbmu.edu.cn (W. Zhang).

https://doi.org/10.1016/j.redox.2025.103736
Received 26 May 2025; Accepted 20 June 2025
Available online 24 June 2025

pathway through regulating vascular glycolysis reprogramming, highlighting the therapeutic potential of targeting SIRT6 in the management of diabetic angiopathy.

1. Introduction

Type 2 diabetes mellitus (T2DM), a chronic metabolic disorder characterized by insulin resistance or relative insulin deficiency, leads to persistent hyperglycemia and hyperlipidemia [1,2]. These metabolic disturbances lead to multi-organ dysfunction, including diabetic angiopathy, which emerges as a major vascular complication and a leading cause of morbidity and mortality in diabetic patients [3,4].

Diabetic angiopathy is characterized by sustained vascular smooth muscle cell (VSMC) remodeling and progressive vascular dysfunction, primarily driven by chronic metabolic stress [5,6]. VSMCs are associated with exceptionally high energy requirements, thereby requiring sustained reliance on dynamic flux through glycolytic pathways to maintain contractility and relaxation processes [7,8]. Furthermore, under physiological conditions, glucose in VSMCs is processed via glycolysis, mitochondrial oxidative phosphorylation, and glycogen synthesis [9,10]. However, elevated glucose and fatty acid levels stimulate a phenotypic switch of VSMCs from a contractile to a synthetic/proliferative phenotype in T2DM, accompanied by enhanced mitotic activity, excessive proliferation, and increased migratory capacity [11,12]. Despite increasing evidence linking glycolytic reprogramming to diabetic vascular remodeling [13,14], the precise molecular mechanisms governing glycolysis overactivation and its role in VSMC proliferation-associated vascular remodeling remain to be elucidated.

The impairment of nicotinamide adenine dinucleotide (NAD^+), as a crucial intracellular metabolite, is the pivotal inducement for VSMC proliferation [15,16]. Members of the sirtuin (SIRT) family are NAD^+-dependent deacetylases, which are closely associated with cardiovascular diseases [15,17]. Among them, SIRT6 is regarded as an indispensable regulator of metabolic reprogramming for diverse biological processes. Notably, previous studies on SIRT6 have primarily elucidated its nuclear role in suppressing glycolysis-related gene expression via deacetylation of histone H3 at lysine 9 (H3K9ac) and lysine 56 (H3K56ac) [18,19]. This epigenetic regulation effectively reduces cellular glucose uptake and glycolytic flux, positioning nuclear SIRT6 as a critical transcriptional repressor of metabolic reprogramming. Impressively, recent studies reported the extranuclear presence of SIRT6 in cytoplasmic compartments, e.g., the endoplasmic reticulum [20], stress granules [21], and autophagosomes [22]. This raises the possibility that cytoplasmic SIRT6 contributes to disease pathogenesis. Regrettably, the nuclear export process of SIRT6, its targeting mechanisms, and the functional consequences of its cytoplasmic localization remain unclear.

Hydrogen sulfide (H_2S), a gaseous mediator with cardiovascular protective effects, regulates target proteins via S-sulfhydration [23,24]. Exogenous H_2S supplementation can mitigate cardiovascular damage in diabetic individuals (e.g., hypertension, cardiac ischemia-reperfusion injury, and atherosclerosis) caused by endogenous H_2S deficiency [23,25,26]. However, the impact of H_2S on SIRT6 expression, especially on the expression and mechanism of cytoplasmic SIRT6, remains elusive. This hinders the development of targeted therapies for diabetic patients.

To tackle this issue, two models of diabetic angiopathy were utilized in this study, including leptin receptor gene knock-out (*db/db*) mice and high-fat diet (HFD)/streptozotocin (STZ) treated rats, to elucidate the role of cytoplasmic SIRT6 in vascular glucose metabolism. Our research reveals a novel mechanism through which hyperglycemia and hyperlipidemia impair SIRT6 S-sulfhydration, promote oxidative stress, and drive SIRT6 cytoplasmic translocation via Importin 13 (IPO13). In diabetic VSMCs, SIRT6 interacts with ENO3, a key glycolytic enzyme, enhancing its activity. This accelerates glycolysis reprogramming and leads to aberrant VSMC proliferation. H_2S supplementation restores SIRT6 S-sulfhydration at cysteine 141 (C141), restrains cytoplasmic localization of SIRT6, thereby suppressing ENO3 activity, ameliorating glycolysis reprogramming, and counteracting VSMC proliferation. Given its role in vascular homeostasis, it may protect against glycolysis reprogramming in diabetic angiopathy, offering a new theoretical basis for disease intervention.

2. Materials and methods

2.1. Study participants

For our research, we enrolled participants who were either normoglycemic or had comorbid diabetes. Hyperglycemia is characterized by fasting glucose 7.8 mmol/L, or taking antidiabetic agents for T2DM treatment. Six individuals underwent renal tumor surgery after the assessment of surgical eligibility at the Department of Urology, the First Affiliated Hospital of Harbin Medical University. Renal vascular tissues were harvested during urological procedures, with aliquots snap-frozen at −80 °C or fixed in 4 % paraformaldehyde (PFA) and stored at 4 °C for subsequent analysis. All patients who participated in the study were provided written informed consent. This study was approved by the Institutional Review Board of Harbin Medical University.

2.2. Animal models

Type 2 diabetes mellitus (T2DM) model was established using homozygous leptin receptor-deficient (*db/db*) mice with equal numbers of males and females, while heterozygous (*db/m*) mice served as controls. They were kept in a sterile environment with a stable temperature of 22 °C, a humidity level of 55 %, and a 12-h light/dark cycle. Additionally, GYY4137 was administered through intraperitoneal injections for 4 weeks (133 μM/kg/day). The injections commenced when the mice were 8 weeks old.

Equal numbers of 220–250 g SD rats of both sexes were used in this experiment. The animals were kept in a controlled environment with a 12:12 light/dark cycle and stable humidity and temperature conditions. They were randomly assigned to either the normal control group, which received standard chow, or the high-fat diet (HFD) group. After one month of feeding to establish insulin resistance, insulin deficiency was induced in the HFD group by administering 35 mg/kg/day of STZ by intraperitoneal injection, freshly prepared in 0.1 M sodium citrate buffer, pH 4.5, for three consecutive days. The control group received an equivalent volume of citrate buffer. Seven days after the STZ injection, the rats were assessed for diabetes based on blood glucose levels; levels above 16.7 mM were indicative of diabetic conditions. The HFD/STZ rats were then divided into the HFD/STZ group and the HFD/STZ + GYY4137 group, and GYY4137 was injected intraperitoneally at a dose of 133 μM/kg/day for 12 weeks.

All animal experiments were conducted according to the guidelines of the Ethics Committee of Harbin Medical University.

2.3. Cell culture

Primary rat VSMCs were isolated from the thoracic aortas of male Sprague-Dawley rats (weight 150–180 g) using a tissue-block-based adherence subculture method. HEK293T cells (RRID: CVCL_0063) were purchased from Yeasen. MOVAS cells (RRID: CVCL_0F08) were obtained from Cyagen Biosciences Inc. All the cells were cultured in DMEM (with 10 % FBS) and incubated at 37 °C in a humidified incubator with 5 % CO2. All cells were contamination-free. Cell passaging was performed at 80–90 % confluence, and drug treatments were

administered at 50–60 % confluence in the culture medium over 24 h. Vascular smooth muscle cells were randomly divided into following groups: H_2O_2 (200 μM), Control, HG + Pal (glucose 40 mM, palmitate 200 μM, Sigma), HG + Pal + GYY4137 (100 μM, Selleck), HG + Pal + NaHS (sodium hydrosulphide 100 μM, Sigma), HG + Pal + NAC (100 μM), HG + Pal + Nicotinamide (200 μM). Drugs were added to the cultured medium directly. HG and palmitate were used to mimic hyperglycemia and hyperlipidemia conditions.

2.4. Transcriptomics

Transcriptomics was assessed by Biomarker technologies Co.,Ltd. Total RNA was extracted from vascular smooth muscle cells (VSMCs) in the control, HG + Pal, and HG + Pal + GYY4137 treatment groups using TRIzol reagent (Invitrogen). Sequencing libraries were generated using the NEBNext UltraTM. RNA libraries were constructed from 1 μg total RNA per sample using the NEBNextRUltraTM RNA Library Prep Kit (NEB, USA) according to the manufacturer's guidelines. Indexed libraries were clustered on a cBot system (Illumina) with the TruSeq PE Cluster Kit v4 and sequenced on an Illumina platform to generate paired-end reads.

2.5. Single nuclei RNA sequencing (snRNA-seq)

Single Nuclei RNA Sequencing was conducted by Biomarker technologies Co.,Ltd. Single-cell nuclei were extracted from *db/m* mice and *db/db* mice, and nuclear transcriptome libraries were constructed using the 10x Genomics platform via microfluidic-based droplet encapsulation, barcoding, and high-throughput nuclear capture, followed by sequencing on the Illumina platform.

2.6. Proteomics

Proteomic analyses were performed by Jingjie PTM BioLab Co. Ltd. (Hangzhou, China). Lysates from *db/m* mice and *db/db* mice were centrifuged, and supernatants were processed via acetone precipitation. Proteins were resuspended in TEAB, trypsin-digested overnight, reduced with DTT, and alkylated with IAA. Peptides were separated on an EASY-nLC 1200 system using a formic acid/acetonitrile gradient and analyzed on an Orbitrap Exploris 480 mass spectrometer. Data-independent acquisition (DIA) mode was employed with high-resolution MS1 scans, and HCD fragmentation was applied for MS/MS.

2.7. Liquid chromatography-tandem mass spectrometry (LC-MS/MS) analysis

LC-MS/MS analyses were conducted by Jingjie PTM BioLab Co. Ltd. (Hangzhou, China). Aortic tissue samples were trypsinized, and digested peptides were separated on a NanoElute UHPLC system with a binary gradient of solvent A (0.1 % formic acid, 2 % acetonitrile in water) and B (0.1 % formic acid in acetonitrile). Peptides were analyzed via a TimsTOF Pro mass spectrometer in PASEF mode, with MS/MS spectra acquired and processed using MaxQuant software. Post-translational modifications (S-sulfhydration and acetylation) were identified at a false discovery rate (FDR) < 1 %.

2.8. Analysis of isotopic labeling in metabolomics

A chronic indwelling catheter was surgically implanted into the right jugular vein of mice. Following a 6 h fasting period, [U–^{13}C] glucose (MCE) was infused at 20 mg/kg/min (150 mL/h). Tissues were collected, and arterial blood was drawn for serum preparation. LC-MS/MS analysis was performed, followed by metabolic flux analysis using isotopomer spectral modeling.

2.9. Immunohistochemistry (IHC)

Deparaffinized vascular sections were rehydrated through graded ethanol. Antigen retrieval was performed, followed by endogenous peroxidase blockade with 3 % H_2O_2. Non-specific binding was inhibited with serum matching the secondary antibody species. Sections were incubated overnight at 4 °C with primary antibodies: anti-CSE (Proteintech, 1:200), anti-CBS (Proteintech, 1:200), and anti-3-MST (Abclonal, 1:200). After washing, HRP-conjugated secondary antibodies were applied. Protein expression was visualized using DAB chromogen, followed by hematoxylin counterstaining, dehydration, and coverslip mounting. Staining intensity was analyzed microscopically.

2.10. Cell migration assay

Primary rat aortic VSMCs were cultured in 24-well plates for 24 h. A scratch wound was made in the monolayer using a 200 μL sterile pipette tip. Cells were then treated with HG + Pal for 24 h, and wound closure was monitored at 0 and 24 h via phase-contrast microscopy. The migration index, defined as the percentage of migrated cells relative to the initial wound area, was quantified using ImageJ software.

2.11. Co-immunoprecipitation-mass spectrometry (Co-IP-MS) analysis

The co-immunoprecipitated protein was isolated from the aortic tissues of *db/db* mice with the SIRT6 antibody. Immunoprecipitated complexes were separated via SDS-PAGE and stained with Coomassie Blue for Co-IP-MS analysis. Gel slices were digested with 1 μg trypsin in 100 mM TEAB and 1 mM CaCl2 at 37 °C for 16 h. The resulting peptide mixture was collected, lyophilized, and subsequently analyzed by nanoflow liquid chromatography-tandem mass spectrometry (nLC-MS/MS) using an EASY-nLC™ 1200 UHPLC system (Thermo Fisher Scientific) coupled to a Q Exactive™ HF-X hybrid quadrupole-Orbitrap mass spectrometer (Thermo Fisher Scientific). For database searching, fragment spectra from individual fractions were separately analyzed against the reference proteome using Proteome Discoverer 2.

2.12. Isolation of nucleus and cytoplasm

The nuclei and cytoplasm of vascular tissues and vascular smooth muscle cells (VSMCs) were separated using the Nucl-Cyto-Mem Preparation Kit (Applygen, China) according to the manufacturer's instructions. The protein concentration in the nuclear fractions was measured using the BCA Protein Assay Kit (Solarbio). Equal protein amounts were then subjected to Western blot analysis, with Lamin B1 serving as a nuclear marker.

2.13. Overexpression of CSE

Adeno-associated virus (AAV) expressing CSE was procured from Cyagen Biosciences Inc. (Guangzhou, China). The purified AAV-SIRT6 was administered through intravenous injection into mice via the tail vein.

2.14. Real-time quantitative reverse transcription PCR (RT-qPCR)

Quantitative real-time polymerase chain reaction (RT-qPCR). Total RNA was extracted from primary rat aortic VSMCs using TRIzol reagent (Invitrogen) and reverse transcribed (1000 ng) into cDNA using Hifair® II 1st Strand cDNA Synthesis Kit (Yeasen) according to the manufacturer's instructions. SYBR Green Master Mix (Yeasen) was used for quantitative PCRs. LightCycler 96 System (Roche, Switzerland) was used to test changes in the fluorescence of SYBR Green. Primers used for qPCR, purchased from Sangon, are listed. The expression levels of genes were determined using the $2^{-\Delta\Delta Ct}$ method.

2.15. Duolink in situ proximity ligation assay (PLA)

In situ proximity ligation assay (PLA) was conducted following the manufacturer's protocol using the commercially available Duolink in Situ Red Detection Kit (Sigma-Aldrich). In situ proximity ligation assay was performed as follows: cells were plated on glass-bottom dishes, washed twice with PBS, fixed with 4 % paraformaldehyde for 15 min at room temperature, and blocked with blocking buffer for 1 h at 37 °C. Subsequently, cells were washed twice with PBST (PBS containing 0.1 % Tween 20) and incubated overnight at 4 °C with primary antibodies diluted in Duolink Antibody Diluent: mouse-derived anti-ENO3 (Santa Cruz Biotechnology) and rabbit-derived anti-SIRT6 (Proteintech). Next, the cells were washed three times with Wash Buffer A. Subsequently, secondary probes, including anti-mouse-PLUS and anti-rabbit-MINUS, conjugated to oligonucleotides, were prepared as 1:5 working dilutions in Antibody Diluent. Samples were incubated with a secondary probe solution at 37 °C for 1 h, followed by Wash Buffer A rinses and subsequent addition of 40 μl ligation mix. Following a 30 min incubation at 37 °C, samples were rinsed with Wash Buffer A and subsequently treated with 40 μL amplification mix for 100 min under identical thermal conditions. Following three stringent washes with Wash Buffer B, samples were mounted with 50 μl DAPI-supplemented Duolink in Situ Mounting Medium and subjected to fluorescence imaging, which was quantified by ImageJ.

2.16. Association analysis between SIRT6 and vascular diseases

Disease-associated genes for aortic aneurysm, aortic dissection, and atherosclerosis were retrieved from the MalaCards database. Pearson correlation analysis was performed between SIRT6 and other genes using the atherosclerosis microarray dataset (GSE28829).

2.17. Enrichment analysis of differentially expressed genes (DEGs) in HUVECs

RNA sequencing data of HUVECs were obtained from the NCBI Gene Expression Omnibus (GEO) repository under accession Series GSE213425. Differentially expressed genes (DEGs) between the two groups were identified, and Gene Ontology (GO) enrichment analysis was performed to characterize their functional annotations.

2.18. Detection for pyruvate

Pyruvate were detected by commercially available kits (Solarbio). In brief, a standardized calibration curve for pyruvate quantification was established following the manufacturer's protocol in the assay kit. The supernatant was collected after centrifugation at 8000*g* for 10 min. The supernatant (75 μL) was combined with 25 μL of Reagent 1 from the Kit and incubated for 2 min, followed by the addition of 125 μL of Reagent 2 from the Kit. The absorbance at 520 nm was quantified using a microplate reader to determine pyruvate concentration in accordance with the established calibration curve.

2.19. Detection for lactic acid

Lactate acid (LA) Assay Kit (Solarbio) was used to measure the levels of LA. Lactic acid production was measured using a microplate reader. Cells (1×10^4) were cultured overnight in 12-well plates, followed by 1 h serum-free medium incubation. Supernatants were collected and lactate levels were quantified at 570 nm with a microplate reader.

2.20. Measurement of H_2O_2 concentrations

The intracellular and nuclear H_2O_2 concentrations in VSMCs were quantified using H_2O_2 Assay Kit (Solarbio) following the manufacturer's instructions. Absorbance measurements at 415 nm were obtained using a microplate reader and calculated H_2O_2 concentration.

2.21. Generation of knockout cell lines with CRISPR-Cas9

Sirt6 knockout cells were created using the CRISPR-Cas9 system in Cyagen Biosciences Inc. MOVAS cells were transiently transfected with a plasmid carrying the guide DNA for *Sirt6* and then were seeded into a 96-well plate to form monoclines. Knockout clones were screened by PCR and verified by Sanger sequencing. The forward strand of guide sequence for *Sirt6* was: TGCCTGCAGGAACAGCACTC-TGG, and the reverse strand was: TGCCTGCAGGAACAGCACTC-TGG.

2.22. Measurement of H_2S levels

Hydrogen sulfide levels in *db/db* mice and HFD/STZ rats were measured using the 7-azido-4-methylcoumarin probe (C7Az, Sigma) under 720 nm laser excitation, and visualized with a fluorescence microscope (Olympus, XSZD2).

2.23. Immunofluorescence

Cells were seeded onto coverslips at a density of about 8000 cells per square centimeter. They were fixed with paraformaldehyde for 30 min, permeabilized for 1 h at room temperature, and then incubated with primary antibodies overnight at 4 °C. Afterward, they were incubated with secondary antibodies for 1 h in the dark and subsequently imaged using a fluorescence microscope (Olympus, XSZD2). Following fixation in 4 % paraformaldehyde, vascular tissues were sequentially dehydrated and embedded in OCT for histological processing. Tissue blocks were flash-frozen in liquid nitrogen and cut into 10~20-μm-thick slices. Subsequently, Tissue sections were mounted onto glass slides and permeabilized with 1 % Triton X-100. After blocking, the samples were incubated with anti-Ki67 (Jingjie, 1:100), anti-Sirt6 (Proteintech, 1:100), anti-MMP9 (Proteintech, 1:100), or anti-PCNA (Proteintech, 1:100) for 1 h at room temperature. Following washes, samples were incubated with secondary antibodies and DAPI and then mounted on a coverslip. Confocal imaging was performed on a ZEISS LSM 900 microscope with confocal modality. The co-localization analysis was performed using ImageJ.

2.24. Co-immunoprecipitation (Co-IP)

Protein samples were incubated with anti-SIRT6 (Proteintech), anti-IPO13 (Proteintech), anti-acetylation (Santa), anti-β-Enolase (Santa), anti-Flag (Abmart), or IgG antibodies (Proteintech) and agarose (Selleck) for 8 h at 4 °C. Cell pellets were collected by centrifugation at 10000*g* for 10 min, washed three times with IP buffer, resuspended in sample buffer, and analyzed by immunoblotting.

2.25. Hematoxylin and Eosin (H&E) staining

The aortic tissues were fixed in 4 % paraformaldehyde overnight, followed by dehydration through a graded series of ethanol washes. After clearing in xylene, the samples were embedded in paraffin and sectioned into slices measuring 5–10 μm in thickness. For H&E staining, the sections were stained first with hematoxylin for 10 min and then with eosin for 2 min. After staining, the samples were washed, dehydrated, and examined.

2.26. Measurement of cell viability

The cell viability of VSMCs was assessed using the CCK-8 assay kit (Biosharp). VSMCs were seeded into a 96-well plate, and after treatment, the CCK-8 reagent was added. The plates were incubated at 37 °C in the dark for 1.5 h to allow viable cells to metabolize CCK-8 into formazan. Absorbance at 450 nm was measured to quantify formazan production.

2.27. Seahorse assay

The glycolytic and mitochondrial functions were evaluated based on the glycolytic proton efflux rate (PER) or oxygen consumption rate (OCR). According to the manufacturer's instructions, PER and OCR were detected using an XF Glycolytic Rate Assay kit (Agilent Technologies) and an XF Mitochondrial Stress Test kit (Agilent Technologies) with a Seahorse Bioscience XF Extracellular Flux Analyzer (Seahorse Bioscience), respectively. VSMCs were seeded into XF96 plates at 5000 cells per well in DMEM and were allowed to adhere for 24 h. The glycolytic rate assay was conducted in phenol red-free XF Base Media supplemented with 5 mM HEPES, 10 mM glucose, 1 mM sodium pyruvate, and 2 mM L-glutamine, and the following inhibitors were added at the final concentrations: 10 μM rotenone/antimycin A and 50 mM 2-deoxy-glycose. The mitochondrial stress test was performed in XF Base Media containing 10 mM glucose,1 mM sodium pyruvate, and 2 mM L-glutamine, and the following inhibitors were added at the final concentrations: 1 μM Oligomycin, 2 μM FCCP, and 1 μM rotenone/antimycin A. Results were analyzed using the WAVE version (Agilent Technologies).

2.28. Measurement of β-enolase activity

The activity of β-enolase (ENO3) was assessed using the β-Enolase Activity Assay Kit (Mei Mian). Briefly, isolated proteins from mice were combined with the provided reagents in a well-mixed manner. Subsequently, β-enolase activity was calculated based on absorbance measurements at 450 nm recorded with a microplate reader.

2.29. Dihydroethidium (DHE), DCFH-DA and MitoSOX staining

Cytosolic and mitochondrial ROS levels in cultured VSMCs, *db/db* mice, and HFD/STZ rats were assessed using 25 μM DHE(Beyotime) with DCFH-DA(Beyotime) at 37 °C for 30 min and 5 μM MitoSOX (Invitrogen) at 37 °C for 20 min, respectively. After incubation, cells, and tissues were washed three times with PBS, and fluorescence intensity was quantified by fluorescence microscopy.

2.30. Biotin switch assays

The biotin switch assay was performed as previously described. Vascular tissues or VSMCs were homogenized in 250 mM HEN buffer (250 mM HEPES, 1 mM EDTA, 0.1 mM neocuproine, 100 μM deferoxamine), and centrifuged at 13000 g at 4 °C for 30 min. Protein lysates (500 μg) were treated with blocking buffer (HEN+2.5 % SDS, 20 mM MMTS) at 50 °C for 25 min (vortexing). After acetone precipitation at −20 °C for 1 h, proteins were resuspended in HEN buffer with 1 % SDS. Biotinylation was performed by adding 4 mM biotin-HPDP (DMSO) for 3 h at 25 °C, followed by streptavidin-agarose bead capture at 25 °C for 3 h. Beads were washed four times with cold HEN buffer, and biotinylated proteins were eluted via boiling in Laemmli buffer, then analyzed by SDS-PAGE and immunoblotting.

2.31. Small interfering RNA or plasmid transfection

The SIRT6 small-interfering RNA (siSIRT6) and IPO13 small-interfering RNA (siIPO13), purchased from Sangon Biotech, were transfected into VSMCs at 70–80 % confluency using Lipofectamine 3000 (Invitrogen). The siRNA plasmid and transfection reagent were complexed for 15 min before cellular delivery. Post-transfection, cells were maintained at 37 °C with 5 % CO_2 for downstream analysis.

2.32. Overexpression of SIRT6

FLAG-tagged wild-type SIRT6 ($SIRT6^{WT}$) in vascular smooth muscle cells (VSMCs), purchased by OBiO, was performed via plasmid transfection with Lipofectamine 3000 (Invitrogen). Cultured VSMCs were pre-treated and transfected with the SIRT6-expressing plasmid under optimized conditions. Following a post-transfection incubation period, cells were harvested and subjected to Western blot analysis to assess SIRT6 protein levels. Plasmids suspended in Ringer's solution were injected via the tail vein in 5–7 s into *db/db* mice.

2.33. Generation of point mutation

FLAG-tagged $SIRT6^{C141A}$ plasmid was obtained from OBiO. We utilized a full-length murine SIRT6 construct containing a C141A (cysteine-to-alanine) point mutation. Subsequently, the plasmid was intravenously injected into mice via the tail vein and transfected into cells in vitro. After 6 h, the medium was replaced with fresh DMEM. Cells were treated at 24 h post-transfection, and target proteins were analyzed by Western blot.

2.34. Statistical analysis

All statistical analyses were performed by Prism (GraphPad). Data are expressed as mean ± standard deviation (SD). Statistical analyses used unpaired t-tests for two-group comparisons and one-way ANOVA for multi-group comparisons, with $P < 0.05$ considered statistically significant. Figures of all proteins were generated by PyMol v.4.6.0 software.

3. Results

3.1. Enhanced proliferation and phenotypic switching of VSMCs drive vascular remodeling in T2DM

To investigate pathological alterations in diabetic angiopathy, we employed *db/db* mice (*db/db*) and high-fat diet/streptozotocin rats (HFD/STZ), using *db/m* mice (*db/m*) and normal-chow diet rats (NCD) as controls. Both *db/db* mice and HFD/STZ rats developed significant hyperglycemia compared to their respective controls (Fig. S1A and B, Supporting Information). To map cell-type-specific alterations in type 2 diabetic aortas, we conducted single-nucleus RNA sequencing (snRNA-seq) on aortic tissue from db/db mice and *db/m* mice (Fig. 1A and Supplementary Fig. 1C and D). After stringent quality control, 2918 nuclei from *db/db* and 3634 nuclei from *db/m* mice were retained. Clustering analysis identified dominated vascular and immune cell populations, including vascular smooth muscle cells (VSMCs), endothelial cells, fibroblasts, B lymphocytes, dendritic cells, thymus-dependent lymphocytes, and macrophages (Fig. 1B). Further subclustering of the VSMC population revealed a distinct proliferative/stress-associated subpopulation that was remarkably enhanced in *db/db* mice (Fig. 1C and D). Differential gene expression analysis identified 161 genes significantly dysregulated in this subpopulation (fold change >2, adjusted $P < 0.05$). Gene ontology (GO) and gene set enrichment analysis (GSEA) demonstrated the enrichment of pathways related to cell proliferation, glucose metabolism, sulfur compound binding, and protein deacetylation (Fig. 1E and Supplementary Fig. 1E). Notably, genes associated with cell proliferation were consistently upregulated (Fig. 1F).

Furthermore, we performed H&E and immunofluorescence (IF) staining for Ki67 on renal arteries from diabetic patients, *db/db* mice, and HFD/STZ rats to validate VSMC proliferation in vivo. In the three models, the medial VSMC layer was thickened (Fig. 1G–I), and Ki67 expression was significantly elevated, indicating increased proliferative activity (Fig. 1J–L). Western blot analysis further confirmed the upregulation of the proliferation marker PCNA in diabetic aortas (Fig. 1M and N). We assessed and quantified cell viability in primary rat VSMCs exposed to high glucose and high palmitate conditions. Our results demonstrated that HG/Pal-treated VSMCs exhibited significantly enhanced viability compared to control groups (Fig. 1O).

Building upon single-nucleus-RNA sequencing data showing reduced

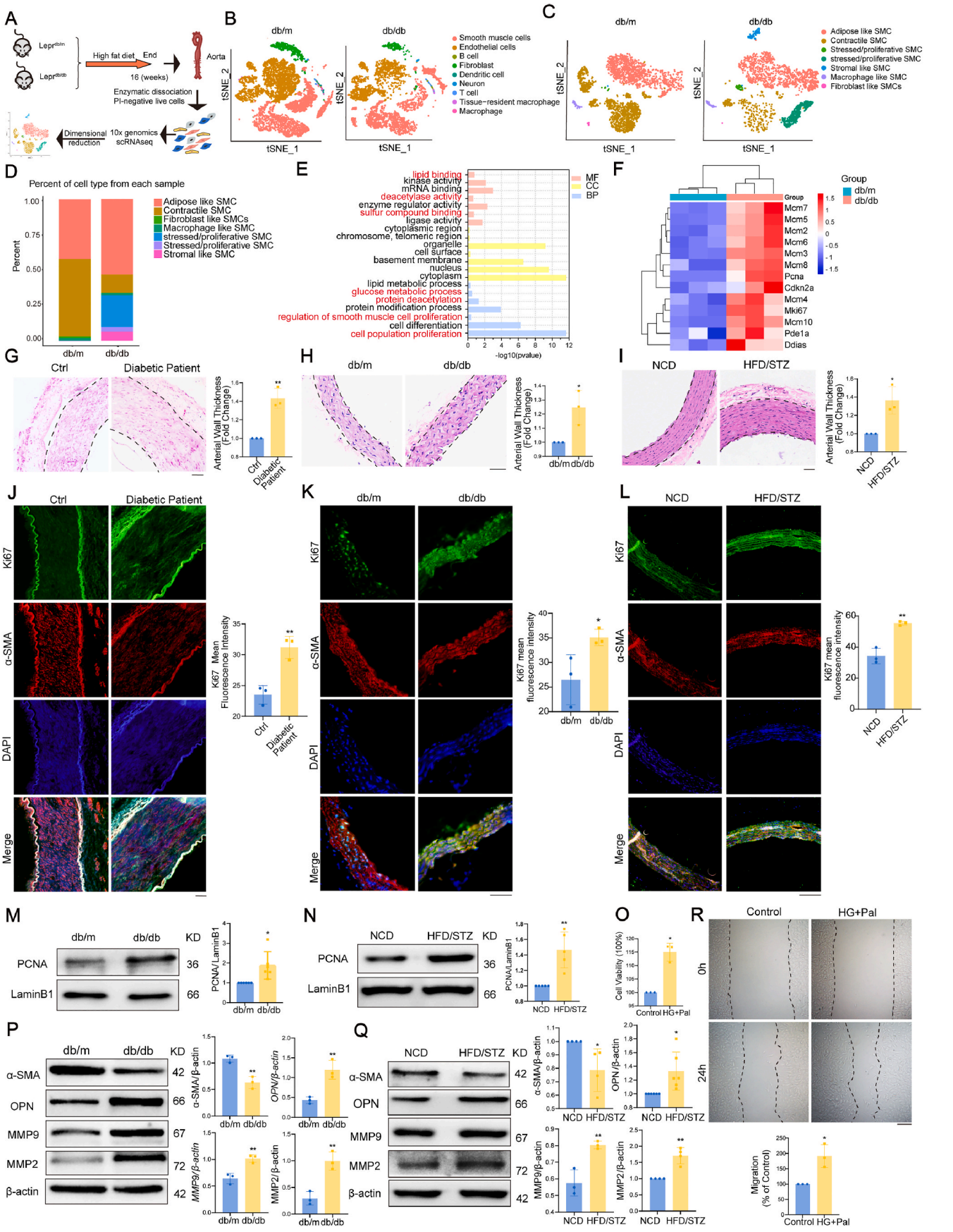

(caption on next page)

Fig. 1. Vascular smooth muscle cells exhibit enhanced proliferation and a contractile-to-synthetic phenotypic switch in type 2 diabetes. (A) Overall experimental procedure. Aortic tissue from three $Lepr^{db/m}$ and three $Lepr^{db/db}$ mice was pooled and enzymatically dissociated to isolate cells, and propidium iodide (PI)-negative cells were subjected to snRNA-seq analysis. (B) tSNE visualization of integrated $Lepr^{db/m}$ and $Lepr^{db/db}$ snRNA-seq analysis. (C) tSNE visualization of proliferative/stress-type subpopulation in db/m and *db/db* mice. (D) Cluster-annotated bar charts showing distributions of $Lepr^{db/m}$ and $Lepr^{db/db}$ mice. (E) Genes were annotated into three main categories: Biological Process (BP), Cellular Component (CC), and Molecular Function (MF). (F) Heatmap showing differentially expressed proliferation-related genes in the two groups. (G–I) Representative photographs of H&E-stained sections of the arterial tissue of diabetic patients (scale bars, 100 μm), *db/db* mice (scale bars, 50 μm), and HFD rats (scale bars, 50 μm). (J–L) Ki67 foci in diabetic patients (scale bars, 100 μm), *db/db* mice (scale bars, 50 μm), and HFD rats (scale bars, 100 μm). (M, N) Protein levels of PCNA in vascular tissues. (O) Cell viability of rat aortic VSMC measured by CCK-8. (P, Q) The expression of VSMC phenotype switch-related protein. (R) Representative images and quantitative analysis of the wound-healing assay in VSMCs. n = 3~6. All quantitative data are demonstrated as mean ± SD from independent experiments. *P < 0.05, **P < 0.01, ***P < 0.001 versus Ctrl, db/m,NCD or Control by unpaired *t*-test.

proportions of contractile VSMCs in *db/db* mice aortas, we subsequently assessed protein levels of contractile markers and synthetic markers to validate VSMC phenotypic switching. Western blot analysis demonstrated that *db/db* mice and HFD/STZ-induced diabetic rats exhibited significant downregulation of the contractile marker α-smooth muscle actin (α-SMA), along with marked upregulation of synthetic phenotype markers including osteopontin (OPN), matrix metalloproteinase 9 (MMP9), and matrix metalloproteinase 2 (MMP2) (Fig. 1P and Q). These molecular changes indicate that VSMCs underwent phenotypic switching in type 2 diabetic aortas. Consistent with previous reports linking vascular injuries (e.g., diabetic vasculopathy and atherosclerosis) to increased migratory capacity during SMC phenotypic switching [27,28], we conducted cell migration experiments. Cell migration assays revealed elevated VSMC migratory capacity under HG/Pal stimulation (Fig. 1R). Taken together, these results suggest that type 2 diabetic aortas undergo significant pathological remodeling characterized by excessive VSMC proliferation, phenotypic switching from contractile to synthetic states, and enhanced migratory capacity.

3.2. Molecular profiling reveals aberrant protein deacetylation and SIRT6 redistribution in diabetic VSMCs

To investigate the mechanisms underlying VSMC proliferation-driven vascular remodeling in type 2 diabetes, we performed transcriptomic sequencing and proteomic sequencing. The transcriptomic analysis of primary rat VSMCs treated with HG/Pal and quantitative proteomics of aortic tissue from *db/db* versus *db/m* mice were performed to expound the molecular signature of diabetic VSMCs. Transcriptomes of HG/Pal-stimulated VSMCs revealed 985 differentially expressed genes (DEGs) compared to the control group ($|\text{fold change}| > 2$, adjusted $P < 0.05$) (Fig. 2A). Subsequent Gene Ontology (GO) enrichment analysis demonstrated significant highlighted pathways governing glucose metabolic process, cell population proliferation, protein deacetylation, and regulation of smooth muscle cell proliferation (Fig. 2B). Subsequently, proteomic profiling detected 160 upregulated proteins and 121 down-regulated proteins in the aortas from *db/db* mice compared with the *db/m* group (Fig. 2C). Subsequent GO enrichment analysis demonstrated significant enrichment of DEGs in pathways related to regulation of smooth muscle cell proliferation, protein deacetylation, glucose metabolic process, and deacetylase activity (Fig. 2D).

Given the consistent enrichment of protein deacetylation pathways, we next quantified global acetylation levels. Both *db/db* vessels and HG + Pal-treated VSMCs displayed a significant increase in total protein acetylation (Supplementary Fig. S2A and B). To determine whether changes in deacetylase expression underlie this hyperacetylation, we analyzed blood RNA-seq from T2DM patients (GSE13760) and observed comparable mRNA levels of all seven sirtuins (SIRT1-7) between patients and controls (Fig. 2E). Likewise, transcript levels of key acetyltransferases and other deacetylases were unchanged in HG/Pal treated cells (Supplementary Fig. 2C and D).

Notably, comparative high throughput sequencing between SIRT6 adenovirus-infected human umbilical vein endothelial cells (HUVECs) and control adenovirus-treated cells revealed significant enrichment of genes associated with cell proliferation through Gene Ontology (GO) analysis (GSE213425) (Supplementary Fig. 2E). Therefore, we focused on SIRT6 to investigate the mechanisms by which it regulates VSMC proliferation-driven vascular remodeling. Furthermore, the Western blot showed downregulation of nuclear SIRT6 in aortas from *db/db* mice and HFD/STZ rats (Fig. 2F and G). Similar findings were obtained in primary VSMCs, corroborating previous results (Fig. 2H). Subsequently, immunofluorescence demonstrated that the nuclear SIRT6 signal was downregulated in human diabetic arteries, db/db mice, HFD/STZ rat vessels, and HG/Pal-treated VSMCs. (Fig. 2I–K and Supplementary Fig. 2F).

The ubiquitin-proteasome system predominantly mediates SIRT6 degradation [29]. Co-immunoprecipitation assays showed enhanced ubiquitination of nuclear SIRT6 in the HG/Pal-treated group (Fig. 2L), suggesting that its depletion in the nucleus is mediated by non-proteasomal mechanisms. Intriguingly, immunofluorescence demonstrated that HG/Pal drives translocation of SIRT6 from the nucleus into the cytoplasm (Fig. 2K), a finding confirmed by Western blot in diabetic patients (Fig. 2M), *db/db* mice (Fig. 2N), HFD/STZ rats (Fig. 2O), and HG + Pal-treated VSMCs (Fig. 2P). Collectively, these findings suggest that following treatment with high glucose and high lipid, the reduced nuclear retention of SIRT6 is not attributable to ubiquitination-dependent proteasomal degradation, but instead results from cytoplasmic translocation of the protein.

3.3. HG/Pal conditions drive oxidative stress-mediated SIRT6 nuclear export via IPO13

The cytoplasmic localization of SIRT6 has been identified in nonalcoholic fatty liver disease (NAFLD), yet its role and regulatory mechanisms in vascular pathophysiology remain poorly understood [30]. Given that cytoplasmic SIRT6 plays a critical role in VSMC proliferation-driven vascular remodeling, we elucidate the underlying molecular mechanism. Proteins transport between the nucleus and cytoplasm via the nuclear pore complex (NPC), guided by nuclear localization signals (NLS) for import and nuclear export signals (NES) for export, with nuclear transport receptors (NTR) and Ran GTPase mechanism facilitating [31]. Reactive oxygen species (ROS), related to nuclear-cytoplasmic transport, mediate shuttling of proteins such as NFκB, GLUT-vesicle, and Nrf2 [32–34]. Therefore, we investigated whether ROS modulates SIRT6 translocation. First, we detected that the aorta from both *db/db* mice and HFD/STZ rats exhibit markedly elevated intracellular ROS levels (Fig. 3A and B and Supplementary Fig. 3A and B). Subsequently, treatment with ROS inhibitors N-acetyl-L-cysteine (NAC) suppressed ROS levels generated by VSMCs in the HG/Pal group (Supplementary Fig. 3C–E). Consistent with impaired redox homeostasis, expression of key antioxidant genes (e.g., *Sod2*, *Cat*) was downregulated in the HG + Pal group, concurrent with enhanced both intracellular and nuclear H_2O_2 accumulation (Fig. 3C–E). To test whether ROS drives SIRT6 redistribution, we examined SIRT6 distribution by Western blot and immunofluorescence after treatment of NAC. Notably, HG/Pal treatment triggered the accumulation of SIRT6 in the cytoplasm, whereas NAC cotreatment largely preserved nuclear SIRT6 localization (Fig. 3F and G).

To identify candidate genes potentially involved in ROS-mediated translocation of SIRT6 to the cytoplasm, RNA sequencing data from dataset GSE108913 were downloaded from the NCBI Gene Expression Omnibus (GEO) repository (Supplementary Fig. S3F). Indeed, we found

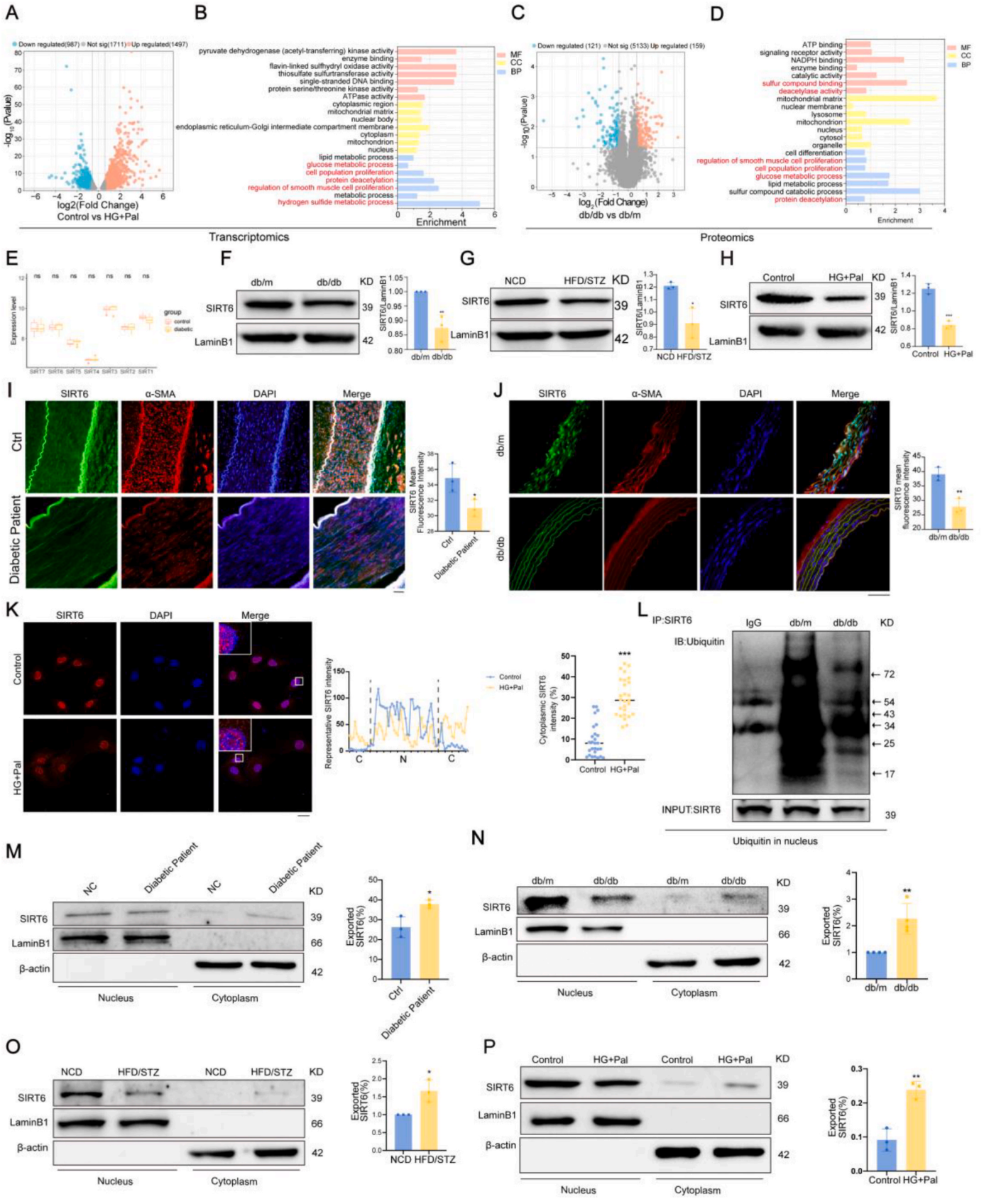

(caption on next page)

Fig. 2. Molecular profiling reveals aberrant protein deacetylation and SIRT6 redistribution in diabetic VSMCs. (A) Differentially expressed genes (DEGs) of transcriptomics between the HG + Pal and control groups are highlighted in the volcano plot. (B) Genes were annotated in three main categories: Biological process (BP), cellular component (CC), and molecular function (MF). (C) Differentially expressed genes (DEGs) of proteomics between $Lepr^{db/db}$ and $Lepr^{db/m}$ are highlighted in the volcano plot. (D) Genes were annotated into three primary Gene Ontology (GO) terms: Biological Process (BP), Cellular Component (CC), and Molecular Function (MF). (E) Wilcoxon rank-sum test was performed on blood RNA-seq data (GSE154881) to identify differentially expressed genes. (F–H) Protein level of SIRT6 in *db/db* mice, HFD rats, and VSMCs. I–K) SIRT6 foci in diabetic patients (scale bars, 100 μm), *db/db* mice (scale bars, 50 μm), and HFD rats (scale bars, 100 μm). (L) Confocal microscopy showing SIRT6 (red) co-localization with nuclei (blue) in VSMCs. Scale bars, 20 μm. (M − P) Protein levels of SIRT6 in nucleus and cytoplasm of diabetic patients, *db/db* mice, HFD/STZ rats and VSMCs. n = 3~4. All quantitative data are demonstrated as mean ± SD from independent experiments. *P < 0.05, **P < 0.01, ***P < 0.001 versus NC, db/m, NCD or Control; $^{\#}$P < 0.05, $^{\#\#}$P < 0.01, $^{\#\#\#}$P < 0.001 versus *db/db*, HFD/STZ or HG + Pal by unpaired *t*-test.

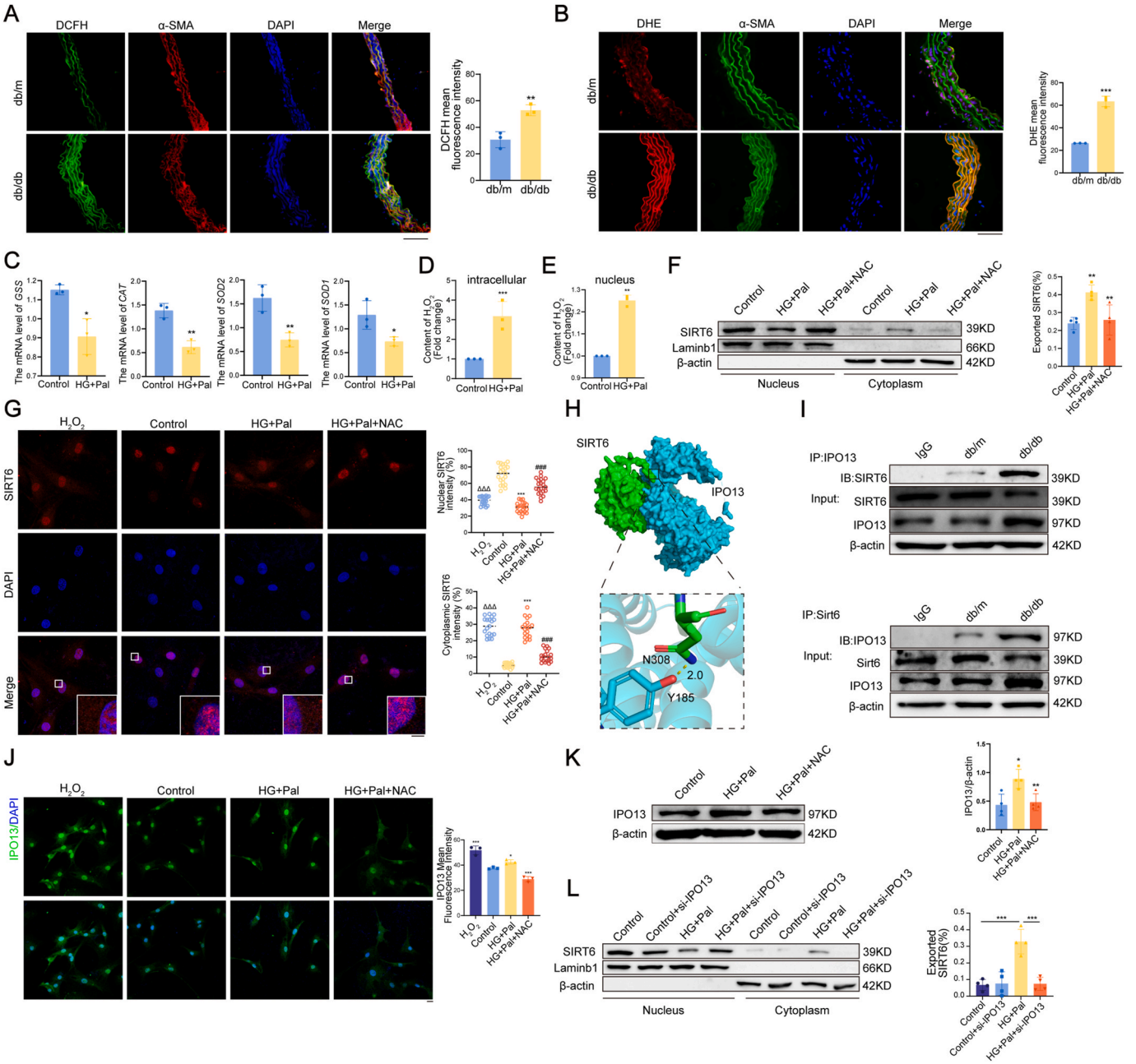

Fig. 3. HG/Pal conditions drive oxidative stress-mediated SIRT6 nuclear export via IPO13. (A, B) The total cytoplasmic ROS levels were detected by using DCFH (green fluorescence) and DHE (red fluorescence). (C) The mRNA level of antioxidant genes. (D, E) The H_2O_2 levels in VSMCs and the nucleus were detected. F) Protein levels of SIRT6 in the nucleus and cytoplasm of VSMCs. (G) Confocal microscopy showing SIRT6 (red) co-localization with nuclei (blue) in VSMCs. Scale bars, 20 μm. (H) Protein docking model of SIRT6 (PDB ID: 6HOY) and the IPO13 (AlphaFold ID: AF-O94829-F1) and the interacting residues in the docked complex. (I) Interaction between SIRT6 and IPO13 was detected by CO-IP. (J) Laser confocal microscopy detection of mean fluorescence intensity and nuclear translocation of IPO13. Scale bar, 20 μm). (K) Protein level of IPO13. (L) Protein levels of SIRT6 in the nuclear and cytoplasmic fractions of VSMCs following transfection with si-IPO13 plasmid. n = 3~4. All quantitative data are demonstrated as mean ± SD from independent experiments. $^{\Delta}$P < 0.05, $^{\Delta\Delta}$P < 0.01, $^{\Delta\Delta\Delta}$P < 0.001 versus H_2O_2; *P < 0.05, **P < 0.01, ***P < 0.001 versus db/m or Control; $^{\#}$P < 0.05, $^{\#\#}$P < 0.01, $^{\#\#\#}$P < 0.001 versus *db/db* or HG + Pal by unpaired *t*-test or ordinary one-way ANOVA.

that Importin 13 (IPO13) was upregulated in the stress-treated group compared to the non-stress group, suggesting that ROS mediates the upregulation of IPO13 expression. Moreover, molecular docking using the HDOCK server revealed a high-affinity interface between SIRT6 and IPO13 (Fig. 3H). Co-immunoprecipitation of aortic lysates confirmed enhanced SIRT6-IPO13 association in *db/db* mice (Fig. 3I). Moreover, high glucose and high palmitate promoted IPO13 protein expression and cytoplasmic translocation in VSMCs, which was downregulated by NAC (Fig. 3J and K).

Next, knockdown of IPO13 with siRNA was employed to assess whether SIRT6 translocates to the cytoplasm in an IPO13-dependent manner. IPO13 siRNA in HG + Pal-treated VSMCs significantly attenuated SIRT6 cytoplasmic accumulation (Fig. 3L and Supplementary Fig. 3G), directly implicating IPO13-mediated ROS-driven translocation of SIRT6 to cytoplasm. Together, these data delineate a novel mechanism whereby diabetic hyperglycemia and hyperlipidemia induce oxidative stress, upregulate expression and cytoplasmic localization of IPO13, and consequently drive the cytoplasmic translocation of SIRT6. These results revealed a redox-sensitive axis of SIRT6 mislocalization integral to diabetic vascular pathology.

3.4. Cytoplasmic accumulation of SIRT6 promotes VSMC proliferation

Because SIRT6 translocated to the cytoplasm under high glucose and high lipid conditions, we evaluated the impact of this translocation. Cells were transfected with SIRT6 siRNA or a SIRT6 overexpression plasmid for 48 h and then exposed to high glucose and high palmitate for 24 h (Supplementary Fig. 4A–C). Based on immunofluorescence staining, we observed that SIRT6 knockdown increased the cytoplasmic translocation of SIRT6 after treatment with HG/Pal, whereas overexpression of SIRT6 suppressed its cytoplasmic accumulation (Fig. 4A and B). High glucose and high lipid elevated VSMC proliferation compared to the control. Notably, the combination of SIRT6 knockdown and HG/Pal treatment further enhanced the expression of Ki67 and PCNA (Supplementary Fig. 4D and E). In contrast, SIRT6 overexpression markedly antagonized HG/Pal-induced VSMC proliferation (Supplementary Fig. S4F and G). To validate these findings in vivo, a SIRT6-overexpressing model in *db/db* mice was established by tail vein injection of a SIRT6-expressing plasmid. After 4 weeks, aortic tissue from SIRT6 overexpression plasmid-treated mice exhibited restored SIRT6 levels (Fig. 4C and D). Notably, in *db/db* mice injected with the SIRT6 overexpression plasmid, the intensity of Ki67 or PCNA fluorescence was reduced, suggesting that SIRT6 overexpression counteracted VSMC proliferation (Fig. 4E and F). Furthermore, attenuation of MMP9 fluorescence intensity in db/db mice injected with the SIRT6 overexpression plasmid revealed that SIRT6 overexpression inhibits VSMC phenotype switch into a synthetic phenotype (Fig. 4G).

To further validate the role of the SIRT6 in VSMC proliferation, we knocked out the *Sirt6* gene (*Sirt6*-KO) in VSMC using CRISPR/Cas9 gene editing (Fig. 4H). We found that knockout of *Sirt6* enhanced cell proliferation and cell viability, which was restored by overexpressing SIRT6 (Fig. 4I–K). *Sirt6*-KO also drove a contractile-to-synthetic phenotype switch, as evidenced by reduced α-SMA and elevated OPN, MMP2, and MMP9 levels, whereas SIRT6 overexpression reversed these changes (Fig. 4L). Overall, these integrated studies indicate cytoplasmic SIRT6 as a pivotal suppressor of VSMC proliferation in T2DM.

3.5. SIRT6-ENO3 interaction elevates glycolysis reprogramming in diabetic VSMCs

To identify how cytoplasmic SIRT6 drives VSMC proliferation, we performed KEGG enrichment on DEG in transcriptomes of HG/Pal-treated VSMCs. Significant enrichment of DEGs in pathways associated with sulfur metabolism, cell cycle, and glycolytic pathways, demonstrated by Kyoto Encyclopedia of Genes and Genomes (KEGG) pathway analysis (Fig. 5A). Among glycolysis-related DEGs, 5 genes were upregulated and 2 genes downregulated upon high glucose and high palmitate stimulation, and these changes were corroborated by RT-qPCR (Fig. 5B and C). Moreover, LC-MS/MS profiling revealed increased acetylation of the glycolytic enzyme ENO3 in T2DM (Fig. 5D). Notably, the intersection of glycolysis-related transcriptomic DEGs and the acetylome yielded ENO3 and LDHA as candidates (Fig. 5E). Subsequently, Western blotting confirmed the reduction of ENO3 protein in HG + Pal group (Fig. 5F).

After confirming that ENO3 expression was upregulated in HG-Pal-induced VSMCs, we went further to investigate potential mechanisms underlying SIRT6-mediated ENO3 protein suppression. For this purpose, co-immunoprecipitation-mass spectrometry (Co-IP-MS) assays were conducted to identify potential binding proteins for SIRT6 from aortas in *db/db* mice (Fig. 5G). As shown in Fig. 5G, an array of proteins could be pulled down by SIRT6 in VSMCs. Considering the previous observation that both the glucose metabolic process and the glycolysis/gluconeogenesis pathway showed significant enrichment in the aortas of *db/db* mice and in HG + Pal-treated VSMCs (Fig. 2A and D and Fig. 5A), we focused mainly on proteins related to glucose metabolic process in Gene Ontology analysis of Co-IP-MS (Fig. 5H). In addition, structure-based docking analysis via HDOCK predicted strong intermolecular interactions between SIRT6 and ENO3 (Fig. 5I). Co-immunoprecipitation from *db/db* mice and HFD/STZ rat aortas confirmed enhanced binding between SIRT6 and ENO3 (Fig. 5J and Supplementary Fig. 5A). Immunofluorescence of VSMCs and HEK293T cells further demonstrated cytoplasmic colocalization of SIRT6 with ENO3 (Fig. 5K and L). Consistent with these results, duolink proximity ligation assay (PLA) revealed cytoplasmic assembly of SIRT6 and ENO3 in the HG + Pal group versus the control group (Fig. 5M).

To analyze whether the ability of SIRT6 to deacetylase ENO3 depended on its enzymatic activity, we used nicotinamide (NAM), which blocks deacetylase and mono-ADP-ribosylase activities of SIRT6. Co-IP assays demonstrated that HG/Pal treatment induced cytoplasmic SIRT6-mediated deacetylation of ENO3, leading to a decreased acetylation level of ENO3, which was restored by NAM (Fig. 5N). Subsequently, SIRT6 overexpression limited its cytoplasmic relocalization and elevated ENO3 deacetylation (Supplementary Fig. 5B). In addition, the accumulation of SIRT6 in the cytoplasm led to ENO3 deacetylation, which resulted in an increase in ENO3 activity in the HG + Pal-treated group (Fig. 5O).

Subsequently, we evaluated downstream metabolites and found that isotopic labeling in metabolomics showed PEP and lactate were markedly elevated in *db/db* mice relative to *db/m* mice (Fig. 5P and Q). Similarly, high glucose and high palmitate treatment increased levels of pyruvate and lactate in VSMCs, indicating enhanced anaerobic glycolysis (Fig. 5R and S), which was confirmed by increased glycolytic proton efflux rate (PER) (Fig. 5T). Finally, knockout of *Sirt6* further enhanced glycolytic flux, which was restored by $SIRT6^{WT}$ (Fig. 5U). Collectively, these data reveal that cytoplasmic SIRT6 binds and deacetylates ENO3 in T2DM, promoting its activity and glycolysis reprogramming in VSMCs.

3.6. Exogenous hydrogen sulfide restores CSE/H_2S signaling and inhibits SIRT6 cytoplasmic translocation in diabetic VSMCs

Building on our earlier findings that exogenous hydrogen sulfide (H_2S) suppresses VSMC proliferation, we further explore the molecular basis of this protective effect [35,36]. The primary enzymes responsible for endogenous H_2S production in mammals are cystathionine γ-lyase (CSE), cystathionine β-synthase (CBS), and 3-mercaptopyruvate sulfurtransferase (3-MST) [37]. To assess the level of H_2S, we first examined the expression of key H_2S-producing enzymes under diabetic conditions. Proteomic analysis revealed a marked downregulation of CSE in HG + Pal group (Fig. 6A). Immunohistochemistry further confirmed diminished CSE expression in the aorta of *db/db* mice and HFD/STZ rats, while levels of CBS and 3-MST remained unchanged (Fig. 6B and

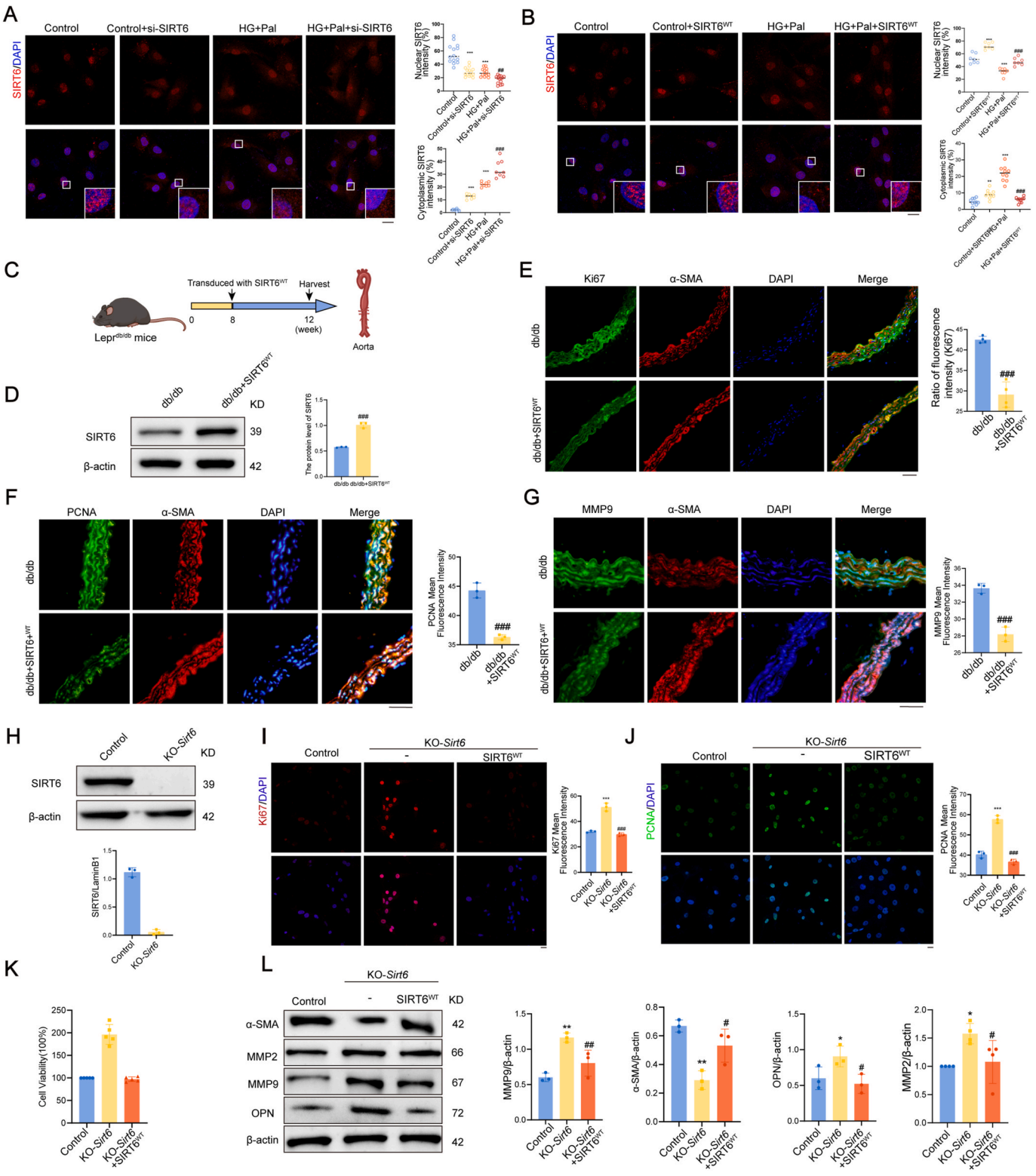

Fig. 4. Cytoplasmic accumulation of SIRT6 promotes VSMC proliferation. (A) Distribution of SIRT6 in VSMCs transfected with si-SIRT6 plasmid. Scale bars, 20 μm. (B) Distribution of SIRT6 in VSMCs transfected with $SIRT6^{WT}$ plasmid. Scale bars, 20 μm. (C) Model of exogenous administration of SIRT6 overexpression plasmid in *db/db* mice. (D) Protein level of SIRT6 after administration of SIRT6 overexpression plasmid in *db/db* mice. (E) Ki67 foci in *db/db* mice. Scale bars, 50 μm. (F) PCNA foci in *db/db* mice. Scale bars, 50 μm. (G) MMP9 foci in *db/db* mice. Scale bars, 50 μm. (H) Protein level of SIRT6 in VSMC. (I) Ki67 foci in KO-*Sirt6* VSMC. Scale bars, 20 μm. (J) PCNA foci in KO-*Sirt6* VSMC. Scale bars, 20 μm. (K) Cell viability of rat aortic VSMC measured by CCK-8. (L) Expression of VSMC phenotype switch-related protein. n = 3~5. All quantitative data are demonstrated as mean ± SD from independent experiments. *P < 0.05, **P < 0.01, ***P < 0.001 versus Control; $^{\#}$P < 0.05, $^{\#\#}$P < 0.01, $^{\#\#\#}$P < 0.001 versus *db/db* HG + Pal or KO-*Sirt6* by unpaired *t*-test or ordinary one-way ANOVA.

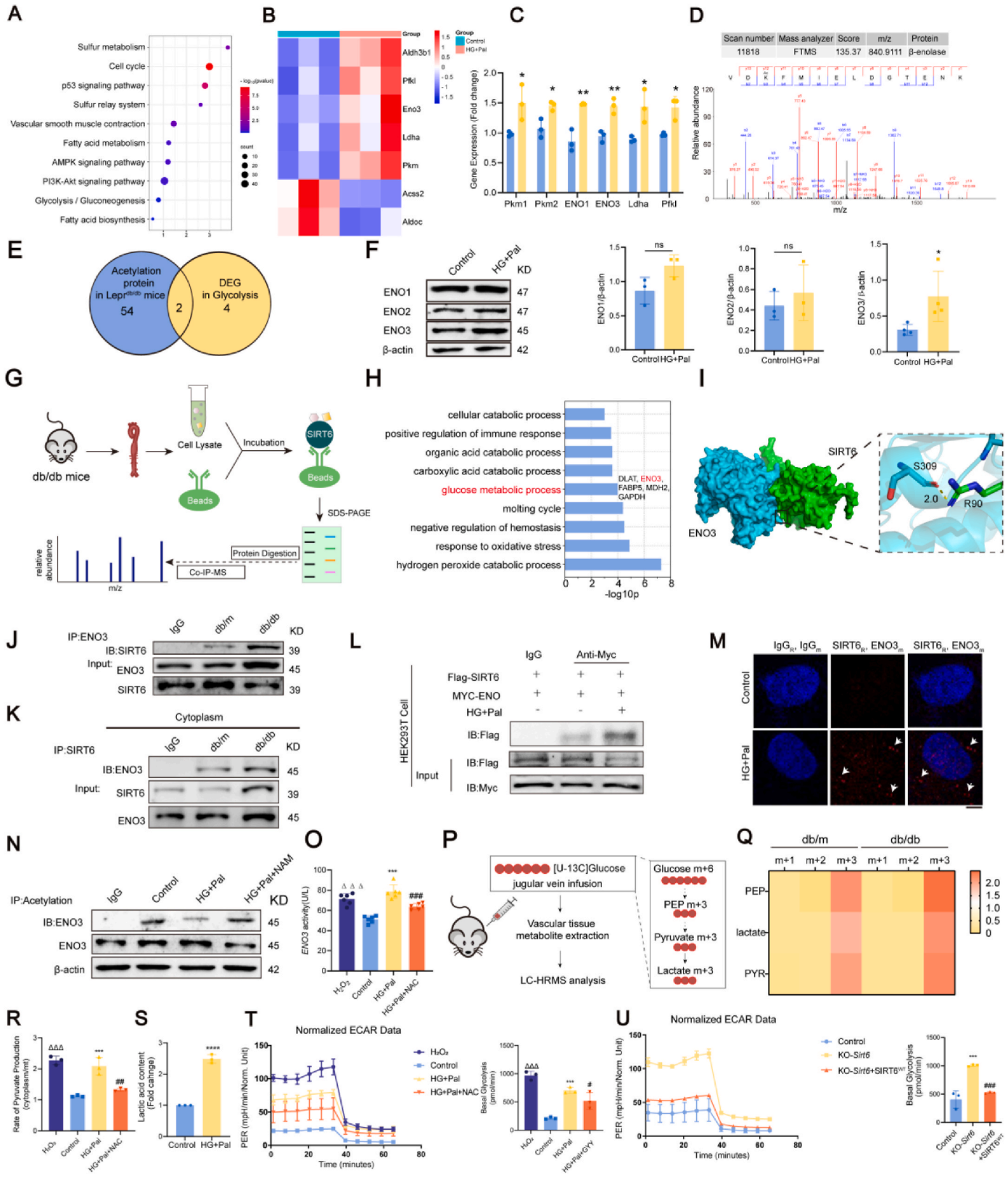

(caption on next page)

Fig. 5. SIRT6-ENO3 interaction promotes glycolytic flux in diabetic VSMCs. (A) Kyoto Encyclopedia of Genes and Genomes (KEGG) enrichment analysis of differentially expressed genes of the control group and HG + Pal treated rat aortic VSMCs identified by RNA-Seq. (B) Heatmap showing differentially expressed glycolysis genes in the control and HG + Pal groups. (C) Gene expression of glycolysis was conducted by RT-qPCR. (D) Acetylation of β-Enolase detected by LC-MS/MS analysis. (E) Venn diagram depicting overlap among the acetylation protein and differentially expressed glycolysis genes by acetylome and RNA-Seq. (F) Protein levels of ENO1, ENO2, and ENO3. (G) Scheme of experiment design of Co-Immunoprecipitation Mass Spectrometry (Co-IP-MS) analysis. Cell lysates extracted from aortic tissues of *db/db* mice were co-immunoprecipitated with SIRT6 antibody, followed by MS detection. (H) Gene Ontology (GO) categories of proteins that were identified in Co-IP-MS in the aortic tissues of *db/db* mice. (I) Protein docking model of SIRT6 (PDB ID: 6HOY) and the ENO3 (AlphaFold ID: AF-P13929-F1) and the interacting residues in the docked complex. (J) Immunoprecipitation assay for detecting the interaction between SIRT6 and ENO3 in *db/db* mice. (K) Interaction between SIRT6 and ENO3 detected by immunoprecipitation assay in the cytoplasm. (L) Detecting the interaction between SIRT6 and ENO3 in HEK293T cells. (M) Representative images of results obtained to investigate SIRT6 and ENO3 interaction by Duolink in situ proximity ligation assay (PLA) assay in VSMCs. The mouse and rabbit IgG antibodies were used as controls. Scale bars, 5 μm. (N) The acetylation level of ENO3 was detected by Co-IP and Western blot analysis. (O) Activity of ENO3 in VSMCs. (P) Schematic illustration of U–^{13}C labeled metabolomics. (Q) Heatmap showing differentially expressed metabolites in the two groups. (R) Rate of pyruvate production in VSMCs. (S) The lactic acid content of rat aortic VSMCs. (T) Normalized and quantification of glycoPER in rat aortic VSMCs. (U) Normalized and quantification of glycoPER in *Sirt6*-KO Movas. n = 3~6. All quantitative data are demonstrated as mean ± SD from independent experiments. $^{\Delta}P < 0.05$, $^{\Delta\Delta}P < 0.01$, $^{\Delta\Delta\Delta}P < 0.001$ versus H_2O_2; $^{*}P < 0.05$, $^{**}P < 0.01$, $^{***}P < 0.001$ versus Control; $^{\#}P < 0.05$, $^{\#\#}P < 0.01$, $^{\#\#\#}P < 0.001$ versus HG + Pal or KO-*Sirt6* by unpaired *t*-test or ordinary one-way ANOVA.

Supplementary Fig. S6A), implicating a selective disruption of CSE-mediated H_2S production in diabetic vasculature. Consistent with these findings, both Western blot and immunofluorescence staining revealed an obvious reduction of CSE in vascular tissues from diabetic patients, *db/db* mice, and HFD/STZ rats compared with their respective controls (Fig. 6C and Supplementary Fig. 6B–D). Similar reductions were observed in vitro VSMC models (Fig. 6D).

Administration of the slow-releasing H_2S donor GYY4137 or the fast-releasing donor NaHS restored CSE levels in HG + Pal treated cells (Fig. 6E). Moreover, fluorescent H_2S probe staining showed reduced H_2S in the vasculature of *db/db* mice and HFD/STZ rats, which was reversed following GYY4137 treatment (Fig. 6F and G). To evaluate the effects of exogenous hydrogen sulfide on cell proliferation, we treated *db/db* mice with GYY4137, indicating that GYY4137 treatment inhibited VSMC proliferation (Fig. 6H). Furthermore, to validate this effect, *db/db* mice were injected via the tail vein with adeno-associated virus (AAV)-mediated overexpression of CSE, which suppressed VSMC proliferation and restored SIRT6 levels in diabetic models (Fig. 6K and Supplementary Fig. 6E). Subsequently, after GYY4137 treatment, cell viability was significantly reduced compared to the HG + Pal group in VSMCs (Supplementary Fig. 6F).

Given the established role of SIRT6 cytoplasmic translocation in driving VSMC proliferation, we next investigated whether H_2S exerts its anti-proliferative effect by modulating SIRT6 subcellular localization. Immunofluorescence and subcellular fractionation analyses revealed that GYY4137 administration suppressed the translocation of SIRT6 from the nucleus to the cytoplasm under HG + Pal conditions (Fig. 6L). Western blotting of nuclear and cytoplasmic fractions from *db/db* mice, HFD/STZ rats, and HG/Pal-treated VSMCs confirmed these observations (Fig. 6M and N and Supplementary Fig. 6G and H). Furthermore, after treatment for high glucose and high lipid, VSMCs exhibited a significant decrease of the contractile marker and increase of the synthetic markers, whereas NaHS and GYY4137 treatment rescued the level of contractile marker and alleviated the level of synthetic markers (Fig. 6O). These findings favored that exogenous H_2S restores CSE/H_2S signaling in diabetic VSMCs, counteracting SIRT6 cytoplasmic translocation, and thereby ameliorating aberrant VSMC proliferation and phenotypic switching.

3.7. H_2S suppresses glycolysis reprogramming via promoting ENO3 acetylation through S-sulfhydration of SIRT6

To further elucidate the molecular mechanism by which H_2S suppresses VSMC proliferation, we assessed the expression of antioxidant genes, indicating that administration of GYY4137 significantly upregulated a set of antioxidant genes (Supplementary Fig. 7A).

Previous evidence highlights S-sulfhydration, a post-translational cysteine modification mediated by H_2S, as a key regulator of protein function and cellular signaling [38]. Biotin switch assays were performed to investigate whether S-sulfhydration of SIRT6 underlies the anti-proliferative effects of H_2S. Notably, GYY4137 treatment restored SIRT6 S-sulfhydration in the aorta of *db/db* mice, HFD/STZ rats, and in VSMCs (Fig. 7A–C and Supplementary Fig. 7B), supporting a role for this modification in vascular homeostasis.

To further delineate downstream mechanisms, KEGG enrichment analysis of DEG in transcriptomic data from VSMCs treated by GYY4137 revealed significant enrichment of glycolytic pathways (Fig. 7D). Specifically, expression of ENO3 was markedly downregulated in the GYY4137-treated group compared to HG + Pal group (Fig. 7E). Western blot analysis confirmed reduced ENO3 protein levels upon both GYY4137 administration and CSE overexpression in *db/db* mice (Fig. 7F and G). Given the nuclear localization of SIRT6 under GYY4137 treatment, we hypothesized that it may regulate ENO3 via deacetylation. Co-IP analyses revealed the interaction between SIRT6 and ENO3 was reduced after administration of GYY4137 (Fig. 7H and Supplementary Fig. 7C). Interestingly, acetyl-proteomic profiling revealed elevated ENO3 acetylation in GYY4137-treated *db/db* mice (Fig. 7I), which was confirmed by Western blot (Fig. 7J). Subsequently, we observed that GYY4137 treatment reduced ENO3 enzymatic activity in HG/Pal-treated VSMCs (Fig. 7K).

To assess the impact on glycolysis, glycolytic proton efflux rate (PER) measurements were performed. GYY4137 administration led to a significant decrease in glycolytic proton efflux rate, as evidenced by reduced extracellular glycoPER and suppressed basal glycolysis (Fig. 7L and M). Correspondingly, intracellular lactate and pyruvate concentrations were decreased, corroborating reduced PER (Supplementary Fig. 7D and E). Subsequently, we assessed mitochondrial function by measuring the oxygen consumption rate (OCR) in VSMCs. GYY4137 treatment restored mitochondrial respiratory parameters, including basal respiration, maximal respiration, and ATP production (Fig. 7N and O), suggesting a metabolic shift from glycolysis toward oxidative phosphorylation. Collectively, these findings reveal that H_2S counteracts VSMC proliferation via antioxidant effects and ROS reduction. Notably, H_2S mediates SIRT6 S-sulfhydration, downregulates the interaction between SIRT6 and ENO3, suppresses ENO3 acetylation, and thereby alleviates glycolysis.

3.8. H_2S modulates VSMC proliferation by modifying SIRT6 at Cys141

To determine the critical site of SIRT6 S-sulfhydration responsible for H_2S-mediated suppression of VSMC proliferation, we employed liquid chromatography-mass spectrometry (LC-MS/MS) coupled with time-of-flight (TOF) detection. Selective S-sulfhydration at cysteine residue 141 (Cys141) of SIRT6 was identified in vascular tissues from GYY4137-treated *db/db* mice (Fig. 8A). Notably, Cys141 is highly conserved across species, suggesting its potential functional significance (Supplementary Fig. 8A). To investigate the role of SIRT6 in the VSMC proliferation, we constructed and transfected a plasmid of SIRT6

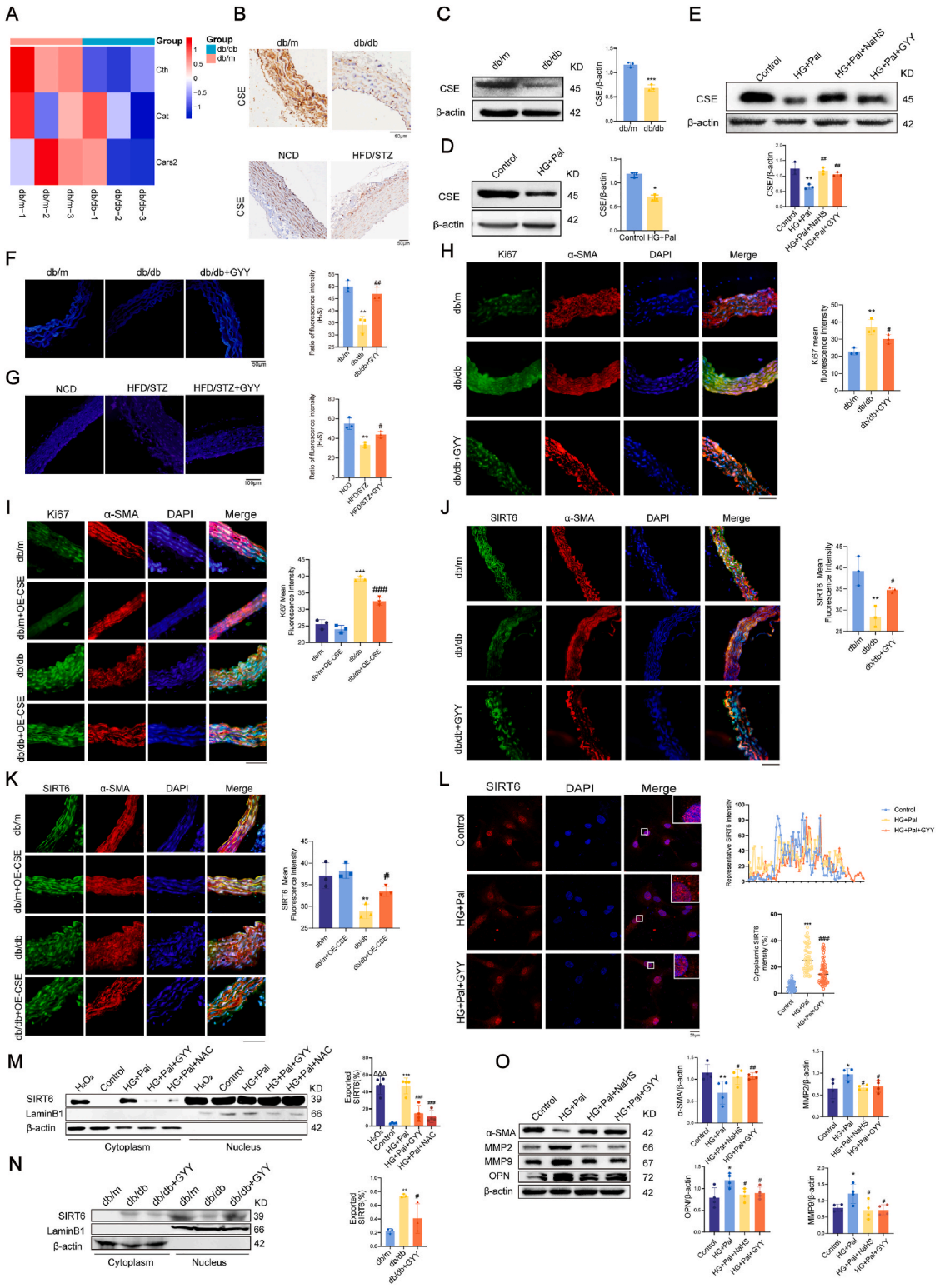

Fig. 6. Exogenous hydrogen sulfide restores CSE/H_2S signaling and inhibits SIRT6 cytoplasmic translocation in diabetic VSMCs. (A) Heatmap showing differentially expressed genes related to hydrogen sulfide synthesis and metabolism in the two groups. (B) Representative immunohistochemistry (IHC) staining images of CSE in the aorta of db/db mice and HFD/STZ rats. Scale bars, 50 μm. (C) Protein level of CSE in *db/db* mice. (D) Protein level of CSE in VSMCs. (E) Protein level of CSE in NaHS and GYY-treated VSMCs. (F) H_2S content detected by 7-azido-4-methylcoumarin (C-7Az) in *db/db* mice. Scale bars, 50 μm. (G) H_2S content detected by C-7Az in HFD/STZ rats. Scale bars, 100 μm. (H, I) Ki67 foci in *db/db* mice. Scale bars, 50 μm. (J, K) SIRT6 foci in *db/db* mice. Scale bars, 50 μm. (L) Confocal microscopy showing SIRT6 (red) co-localization with nuclei (blue) in VSMCs. Scale bars, 20 μm. (M, N) Protein levels of SIRT6 in nucleus and cytoplasm of VSMCs and *db/db* mice. (O) The expression of VSMC phenotype switch-related protein. n = 3~4. All quantitative data are demonstrated as mean ± SD from independent experiments. $^{\Delta}P < 0.05$, $^{\Delta\Delta}P < 0.01$, $^{\Delta\Delta\Delta}P < 0.001$ versus H_2O_2; *P < 0.05, **P < 0.01, ***P < 0.001 versus Control, db/m or NCD; $^{\#}P < 0.05$, $^{\#\#}P < 0.01$, $^{\#\#\#}P < 0.001$ versus HG + Pal, *db/db* or HFD/STZ by unpaired *t*-test or ordinary one-way ANOVA.

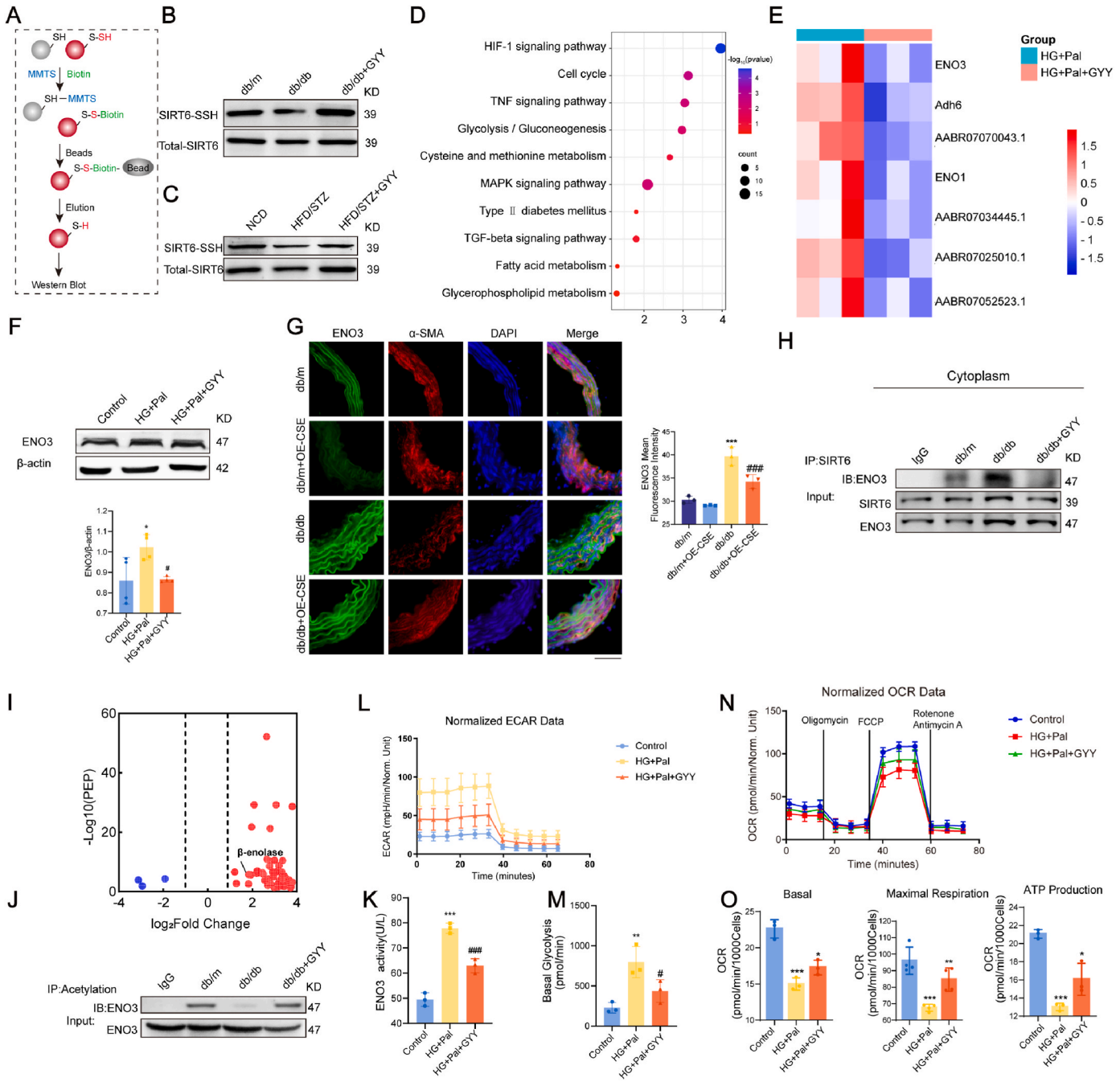

Fig. 7. H_2S suppresses glycolysis via promoting ENO3 acetylation through S-sulfhydration of SIRT6. (A) Model of biotin transformation experiment. (B, C) S-sulfhydration levels of SIRT6 in *db/db* mice and HFD/STZ rats. (D) Kyoto Encyclopedia of Genes and Genomes (KEGG) enrichment analysis of differentially expressed genes of HG + Pal and GYY treated rat aortic VSMCs identified by RNA-Seq. (E) Heatmap showing differentially expressed glycolysis genes in the HG + Pal and GYY groups. (F) Protein level of ENO3. (G) ENO3 foci in *db/db* mice were injected via the tail vein with adeno-associated virus (AAV)-mediated overexpression of CSE. (H) The interaction between SIRT6 and ENO3 in cytoplasm was detected by immunoprecipitation assay. (I) The acetylation level of different proteins detected by acetylome between the *db/db* and *db/db* + GYY groups is highlighted in the volcano plot. (J) The acetylation level of ENO3 was detected by Co-IP and Western blot analysis. (K) Activity of ENO3 in VSMCs. (L) Normalized ECAR of VSMCs. (M) Quantification of ECAR. (N) Normalized OCR of VSMCs. (O) Quantification of ECAR. n = 3~4. All quantitative data are demonstrated as mean ± SD from independent experiments. *P < 0.05, **P < 0.01, ***P < 0.001 versus Control or db/m; $^{\#}$P < 0.05, $^{\#\#}$P < 0.01, $^{\#\#\#}$P < 0.001 versus HG + Pal or *db/db* by ordinary one-way ANOVA.

mutated at cysteine 141 to alanine (C141A) into VSMC and *db/db* mice. As a result, the overexpression of SIRT6 C141A fails to enhance the cysteine S-sulfhydration levels of SIRT6 treated with GYY4137 compared with the HG + Pal group (Fig. 8B). GYY4137 treatment failed to suppress VSMC proliferation in mice expressing the C141A, indicating that Cys141 is essential for H_2S-induced SIRT6 regulation (Fig. 8C–E). In addition, transduction of VSMCs with a plasmid carrying the SIRT6-C141A mutant gene revealed that GYY4137 fails to reverse the translocation of SIRT6 into the cytoplasm (Fig. 8F).

Further mechanistic studies were conducted in SIRT6 knockout VSMCs transfected with either FLAG-tagged wild-type SIRT6 ($SIRT6^{WT}$) or the $SIRT6^{C141A}$ mutant. As expected, the C141A mutant was resistant to S-sulfhydration (Fig. 8G). Furthermore, *Sirt6* knockout enhanced cell viability (Fig. 8H), VSMC proliferation, and glycolytic flux (Fig. 8I and J

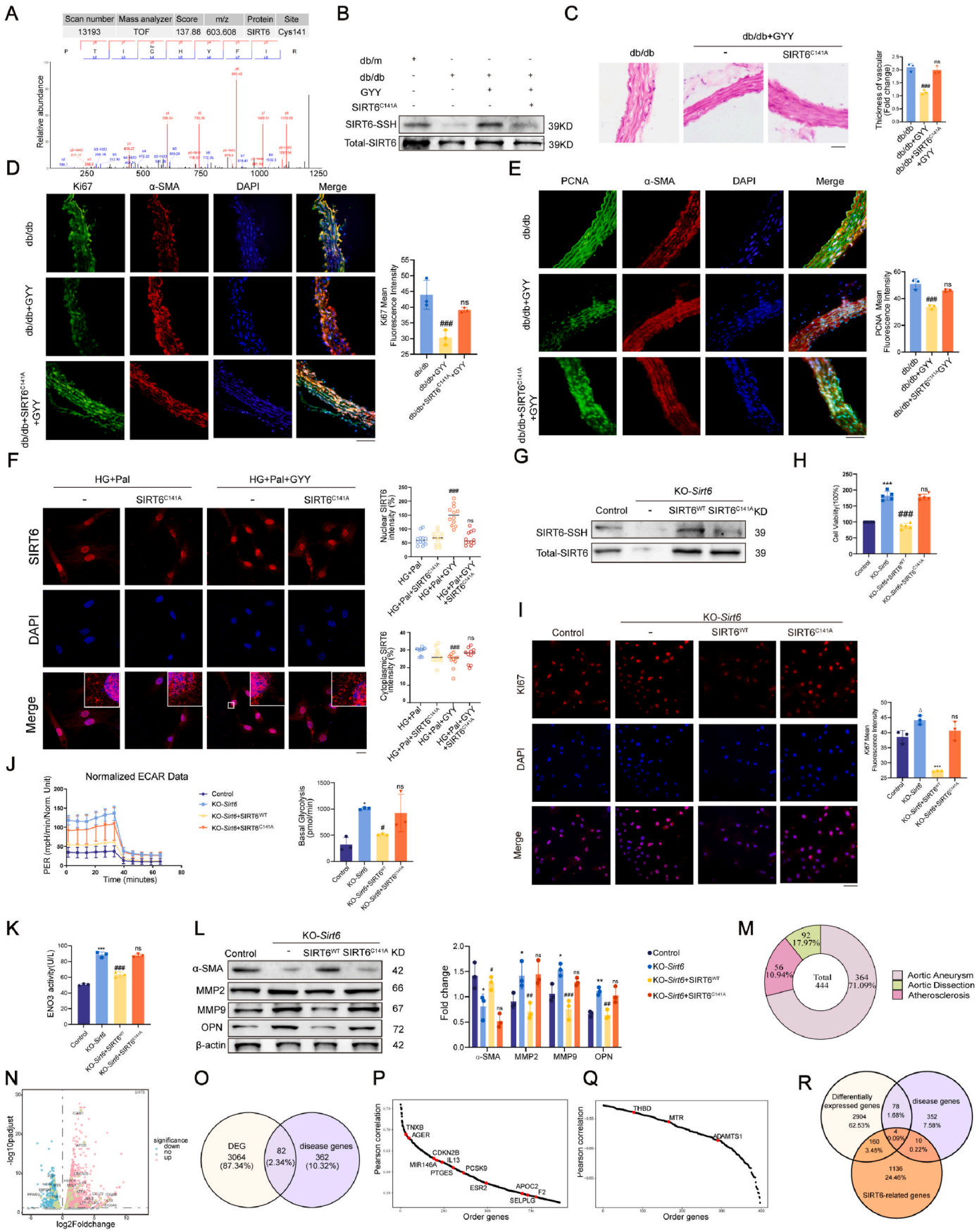

(caption on next page)

Fig. 8. H_2S modulates VSMC proliferation by modifying SIRT6 at Cys141. (A) S-sulfhydration of SIRT6 detected by LC-MS/MS analysis. (B) S-sulfhydration levels of SIRT6 in *db/db* mice. (C) Representative photographs of H&E-stained sections of the arterial tissue. (D) Ki67 foci in *db/db* mice. Scale bars,50 μm. (E) PCNA foci in *db/db* mice. (F) Confocal microscopy showing SIRT6 (red) co-localization with nuclei (blue) in VSMCs. Scale bars, 20 μm. (G) S-sulfhydration levels of VSMCs. (H) Cell viability of rat aortic VSMC measured by CCK-8. (I) Ki67 foci in KO-*Sirt6* VSMCs. Scale bars,50 μm. (J) Normalized and quantification of glycoPER in rat aortic VSMCs. (K) Activity of ENO3 in VSMCs. (L) The expression of VSMC phenotype switch-related protein. (M) Pie charts represent the three disease-related genes for aortic aneurysm, aortic coarctation, and atherosclerosis obtained from the MALAcards database. (N) Volcano plot of differentially expressed genes. Downregulation and upregulation were shown in the blue and red dots, respectively. Data were obtained from the GEO database (GSE 213425). (O) Venn diagram depicting the overlap between expressed genes and disease genes. (P, Q) Pearson correlation of SIRT6 and atherosclerosis-related genes obtained from microarray data (GSE28829). (R) Venn diagram depicting overlap among differentially expressed genes, disease genes, and SIRT6-related genes. n = 3~5. All quantitative data are demonstrated as mean ± SD from independent experiments. *P < 0.05, **P < 0.01, ***P < 0.001 versus Control; $^{\#}$P < 0.05, $^{\#\#}$P < 0.01, $^{\#\#\#}$P < 0.001 versus HG + Pal, *db/db*, KO-*Sirt6* by ordinary one-way ANOVA.

and Supplementary Fig. 8B), accompanied by increased ENO3 enzymatic activity (Fig. 8K), which was restored by overexpressing $SIRT6^{WT}$ but not $SIRT6^{C141A}$. In addition, Western blot showed that the extent of VSMC phenotype switch in the $SIRT6^{C141A}$ group administered GYY4137 was lower than that in the wild-type SIRT6-overexpressing group treated with GYY4137 (Fig. 8L). Overexpression of $SIRT6^{WT}$ reversed HG/Pal-induced pathological phenotypic switching in VSMCs, while the C141A mutant failed to exert this protective effect, reinforcing the functional importance of Cys141 in SIRT6-mediated vascular homeostasis.

To extend these findings to human vascular pathophysiology, we investigated the association between SIRT6 and vascular diseases. A total of 444 disease-associated genes linked to aortic aneurysm, aortic dissection, and atherosclerosis were retrieved from the MalaCards database (Fig. 8M), among which SIRT6 was classified as an aortic aneurysm-related gene. Transcriptome analysis of human venous endothelial cells overexpressing SIRT6 (GSE213425) identified 1768 upregulated and 1368 downregulated genes (FDR <0.05, $|\log_2 FC| > 0$) (Fig. 8N). Of these, 82 overlapped with known vascular disease-associated genes, highlighting SIRT6 as a potential regulatory hub in vascular disease (Fig. 8O). To further assess relationships among genes, Pearson correlation analysis was performed using microarray data (GSE28829). In early-stage intimal thickening lesions, SIRT6 expression positively correlated with 11 disease-associated genes and negatively with 3 others (Fig. 8P and Q). Four vascular disease genes displayed both differential expression and strong correlation with SIRT6-regulated transcriptional signatures (Fig. 8R). Finally, differential expression analysis of aortic dissection samples (GSE147026) confirmed that SIRT6 expression was significantly elevated in pathological tissues compared to normal aortic samples (Supplementary Fig. 8C), further implicating its role in vascular remodeling. Taken together, these results demonstrate that Cys141 is the critical site for H_2S-mediated SIRT6 S-sulfhydration, which governs SIRT6 subcellular localization and its anti-proliferative function in VSMCs. Furthermore, the transcriptional and clinical relevance of SIRT6 underscores its potential as a mechanistic regulator and biomarker for diabetes-associated vascular complications, including aneurysms, dissection, and atherosclerosis.

4. Discussion

The salient findings of this study confirmed that cytoplasmic translocation of SIRT6 promotes glycolysis reprogramming in T2DM. This was supported by data from *db/db* mice, HFD/STZ rats , SIRT6-overexpressing mice, and genetically mutated mouse models. Our data revealed that cytoplasmic SIRT6 promoted glycolysis and VSMC phenotype switch. We also found that cytoplasmic SIRT6 facilitated the activity of ENO3 by deacetylating ENO3 to promote glycolysis reprogramming, therefore exacerbating VSMC proliferation-related vascular remodeling and eventually aggravating T2DM development. This study not only described the critical role of cytoplasmic SIRT6 translocation in T2DM incidence but also unveiled the mechanical potential of targeting cytoplasmic SIRT6 for T2DM prevention.

The highly conserved NAD^+-dependent family of sirtuin deacetylases and mono-ADP ribosyltransferases (sirtuins 1–7) are key epigenetic regulators that control metabolism-associated cell signaling pathways [39]. Nuclear NAD^+-dependent deacetylase SIRT6 has been extensively investigated and is notably recognized for its vital role in orchestrating cardiovascular and metabolic homeostasis, primarily by facilitating histone deacetylation [40,41]. For example, in endothelial cells, SIRT6 suppressed endothelial expression of PPARγ through SIRT6-dependent deacetylation of histone H3 lysine 9 around the PPARγ promoter region to regulate endothelial FA uptake [40]. In VSMCs, SIRT6 protects against thoracic aortic aneurysms by epigenetically inhibiting vascular inflammation and senescence by reducing the H3K9 and H3K56 acetylation [42]; Runx2 was deacetylated by SIRT6 and further promoted nuclear export via exportin 1 (XPO1) to prevent vascular calcification [43]. However, evidence indicates that SIRT6 is also present in the cytoplasm [21,30]. Given that SIRT6 has been traditionally recognized for its nuclear functions, elucidating the precise role of cytoplasmically localized SIRT6 in diabetic angiopathy is important and remains to be investigated.

Reactive oxygen species (ROS), which are correlated with nuclear-cytoplasmic transport, orchestrate the shuttling of a variety of proteins, including NFκB, GLUT vesicle, and Nrf2 [32–34]. Thus, we consider that high-glucose and high-lipid elevate ROS levels, which modulate SIRT6 nuclear export signals, thereby leading to the accumulation of SIRT6 in the cytoplasm. In this study, high-glucose and high-lipid stress promoted the nuclear export of SIRT6 via Importin 13 (IPO13). IPO13, a biportin known to shuttle proteins such as GR and Ubc9 [44,45], is closely associated with responses to stress contributing to cell repair [46]. This study revealed that ROS promote cytoplasmic translocation of SIRT6, a process mediated by the IPO13.

Previous studies have demonstrated that glycolysis is implicated as a significant contributor to diabetic angiopathy [47]. Consequently, we aim to explore whether cytoplasmic SIRT6 exerts a regulatory role in glycolysis in diabetic angiopathy. We present evidence that SIRT6 deacetylated ENO3 by interacting with ENO3, a key glycolytic enzyme that catalyzes 2-PGA to PEP. Previous studies have demonstrated that protein acetylation and deacetylation contribute to changes in protein activity, which affect various pathological processes [48,49]. We demonstrated that SIRT6 deacetylates ENO3, thereby reducing its activity and consequently exacerbating glycolysis reprogramming under hyperglycemic and hyperlipidemic conditions.

One of the most notable findings of our study was the role of H_2S in ameliorating glycolysis reprogramming by targeting SIRT6. H_2S homeostasis is vital for maintaining the physiological functions of various organs, and endogenous H_2S levels are associated with many biological activities, such as diabetes and metabolic dysregulation [50,51]. Previous studies have demonstrated that H_2S ameliorates cardiovascular dysfunction and metabolic disorders [23,52]. In this study, H_2S attenuates VSMC proliferation and the contractile-synthetic phenotypic switch. We assume that the underlying mechanisms may involve multiple pathways. On the one hand, H_2S reduces ROS generation; on the other hand, it enhances the S-sulfhydration of SIRT6 at the C141 residue.

Current studies have limitations. Exogenous hydrogen sulfide (H_2S) inhibits SIRT6 translocation by suppressing ROS and enhancing S-sulfhydration at cysteine 141 residue. However, the mechanism underlying how increased S-sulfhydration suppresses SIRT6 translocation remains

unclear. We hypothesize that the S-sulfhydration modification may alter the molecular conformation of SIRT6, thereby hindering its translocation. Elucidating the associated pathways may further clarify the therapeutic potential of targeting SIRT6 in T2DM.

Taken together, our findings reveal a novel mechanism by which SIRT6 regulates VSMC proliferation in T2DM, connecting metabolic reprogramming to vascular remodeling. We show that hyperglycemic and hyperlipidemic conditions stimulate SIRT6 cytoplasmic translocation via IPO13-dependent nuclear export. This shifts the function of SIRT6 from nuclear epigenetic regulation to cytosolic glycolysis modulation. Cytoplasmic SIRT6 enhances glycolysis by deacetylating ENO3, promoting VSMC proliferation, a key feature of diabetic angiopathy. Importantly, we identify H_2S as a therapeutic agent that restores nuclear SIRT6 retention by attenuating oxidative stress and restoring S-sulfhydration at Cys141. This disrupts ROS production and suppresses ENO3-driven glycolysis.

5. Conclusion

Cytoplasmic SIRT6-mediated deacetylation of ENO3 regulates glycolysis reprogramming and VSMC proliferation-associated vascular remodeling in type 2 diabetic aortas, highlighting the significance of cytoplasm-localized SIRT6 as a novel regulator in this process. Hyperglycemia and hyperlipidemia promote SIRT6 nuclear-to-cytoplasmic translocation via its interaction with the nuclear transport protein Importin 13. Once in the cytoplasm, SIRT6 interacts with and deacetylates ENO3, which enhances its enzymatic activity, thereby exacerbating glycolysis reprogramming and accelerating vascular remodeling. Therapeutically, hydrogen sulfide (H_2S) reduces cytoplasmic translocation of SIRT6 by restoring S-sulfhydration at cystein 141 residue of SIRT6. This suppresses ENO3-mediated glycolysis reprogramming, reduces VSMC proliferation, and restores vascular homeostasis.

CRediT authorship contribution statement

Kemiao Pang: Formal analysis, Investigation, Methodology, Software, Writing – original draft, Writing – review & editing. **Jiayi Huang:** Formal analysis, Investigation, Methodology, Software, Writing – original draft, Writing – review & editing. **Shiwu Zhang:** Formal analysis, Investigation, Methodology, Software, Writing – review & editing, Funding acquisition. **Yinghui Guan:** Data curation, Formal analysis, Investigation, Methodology. **Ning Zou:** Data curation, Formal analysis, Investigation, Methodology. **Jiaxin Kang:** Conceptualization, Software, Validation, Visualization. **Haining Du:** Conceptualization, Software, Validation, Visualization. **Dechao Zhao:** Funding acquisition, Project administration, Resources, Supervision. **Denis V. Abramochkin:** Funding acquisition, Project administration, Resources, Supervision. **Heyu Chen:** Validation, Visualization. **Nan Zhang:** Data curation, Formal analysis. **Yunyan Gu:** Data curation, Formal analysis. **Ning Liu:** Supervision, Validation. **Yining Niu:** Validation, Visualization. **Ziqi Xiong:** Investigation, Methodology, Project administration. **Xueya Zhang:** Investigation, Methodology, Project administration. **Fanghao Lu:** Investigation, Methodology, Project administration. **Huitao Fan:** Funding acquisition, Resources, Supervision, Writing – review & editing. **Jinwei Tian:** Funding acquisition, Resources, Supervision, Writing – review & editing. **Bo Yu:** Funding acquisition, Resources, Supervision, Writing – review & editing. **Shuijie Li:** Formal analysis, Resources, Visualization. **Weihua Zhang:** Conceptualization, Formal analysis, Funding acquisition, Methodology, Resources, Writing – review & editing.

Ethics

All animal experiments were conducted according to the guidelines of the Ethics Committee of Harbin Medical University. All patients participated in the study were provided written informed consent. This study was approved by the Institutional Review Board of Harbin Medical University.

Funding

This work was supported by the National Natural Science Foundation of China (No. 82270359, 82370367), the Natural Science Foundation of Heilongjiang Province (LH2024H009), and the Open Fund of the Key Laboratory of Hepatosplenic Surgery, Ministry of Education, Harbin, China (GPKF202306). Additional support was provided by the Fund of the Key Laboratory of Myocardial Ischemia, Ministry of Education (KF202404), and the Postgraduate Research & Practice Innovation Program of Harbin Medical University (YJSCX2023-04HYD). Scientific Research Project of Provincial Scientific Research Institutes of Heilongjiang Province (Grant CZKYF2024-1-A010).

Declaration of competing interest

The authors declare no conflict of interest.

Acknowledgments

The authors thank Jingjie PTM BioLab Co. Ltd. (Hangzhou, China) for the mass spectrometry analysis.

Appendix A. Supplementary data

Supplementary data to this article can be found online at https://doi.org/10.1016/j.redox.2025.103736.

References

[1] K.P. Zucatti, P.P. Teixeira, L.F. Wayerbacher, G.F. Piccoli, P.E. Correia, N.K. O. Fonseca, et al., Long-term effect of lifestyle interventions on the cardiovascular and all-cause mortality of subjects with prediabetes and type 2 diabetes: a systematic review and meta-analysis, Diabetes Care 45 (2022) 2787–2795, https://doi.org/10.2337/dc22-0642.

[2] J. Xie, M. Wang, Z. Long, H. Ning, J. Li, Y. Cao, et al., Global burden of type 2 diabetes in adolescents and young adults, 1990-2019: systematic analysis of the global burden of disease study 2019, Bmj 379 (2022) e072385, https://doi.org/10.1136/bmj-2022-072385.

[3] N.H. Cho, J.E. Shaw, S. Karuranga, Y. Huang, J.D. da Rocha Fernandes, A. W. Ohlrogge, B. Malanda, IDF diabetes Atlas: global estimates of diabetes prevalence for 2017 and projections for 2045, Diabetes Res. Clin. Pract. 138 (2018) 271–281, https://doi.org/10.1016/j.diabres.2018.02.023.

[4] E.W. Gregg, N. Sattar, M.K. Ali, The changing face of diabetes complications, Lancet Diabetes Endocrinol. 4 (2016) 537–547, https://doi.org/10.1016/s2213-8587(16)30010-9.

[5] J. Shi, Y. Yang, A. Cheng, G. Xu, F. He, Metabolism of vascular smooth muscle cells in vascular diseases, Am. J. Physiol. Heart Circ. Physiol. 319 (2020) H613–h631, https://doi.org/10.1152/ajpheart.00220.2020.

[6] S.H. Cao, R.Y. Ma, T. Cao, T. Hu, S. Yang, Z.Y. Ren, et al., PKM2 crotonylation reprograms glycolysis in VSMCs, contributing to phenotypic switching, Oncogene (2025), https://doi.org/10.1038/s41388-025-03353-9.

[7] E.V. Dolmatova, K.K. Griendling, Platelet microRNAs and vascular injury, J. Clin. Investig. 129 (2019) 962–964, https://doi.org/10.1172/jci127580.

[8] Y.Q. Dou, P. Kong, C.L. Li, H.X. Sun, W.W. Li, Y. Yu, et al., Smooth muscle SIRT1 reprograms endothelial cells to suppress angiogenesis after ischemia, Theranostics 10 (2020) 1197–1212, https://doi.org/10.7150/thno.39320.

[9] L.Y. Wang, C.L. Hung, Y.R. Chen, J.C. Yang, J. Wang, M. Campbell, et al., KDM4A coactivates E2F1 to regulate the PDK-dependent metabolic switch between mitochondrial oxidation and glycolysis, Cell Rep. 16 (2016) 3016–3027, https://doi.org/10.1016/j.celrep.2016.08.018.

[10] Z.Y. Lu, J. Qi, B. Yang, H.L. Cao, R.Y. Wang, X. Wang, et al., Diallyl trisulfide suppresses angiotensin II-Induced vascular remodeling via inhibition of mitochondrial fission, Cardiovasc. Drugs Ther. 34 (2020) 605–618, https://doi.org/10.1007/s10557-020-07000-1.

[11] A. Vallée, R. Guillevin, J.N. Vallée, Vasculogenesis and angiogenesis initiation under normoxic conditions through Wnt/β-catenin pathway in gliomas, Rev. Neurosci. 29 (2018) 71–91, https://doi.org/10.1515/revneuro-2017-0032.

[12] W. Zhou, X. Yuan, J. Li, W. Wang, S. Ye, Retinol binding protein 4 promotes the phenotypic transformation of vascular smooth muscle cells under high glucose condition via modulating RhoA/ROCK1 pathway, Transl. Res. 259 (2023) 13–27, https://doi.org/10.1016/j.trsl.2023.03.004.

[13] Y. Luo, X. Qi, Z. Zhang, J. Zhang, B. Li, T. Shu, et al., Inactivation of malic enzyme 1 in endothelial cells alleviates pulmonary hypertension, Circulation 149 (2024) 1354–1371, https://doi.org/10.1161/circulationaha.123.067579.
[14] I. Subudhi, P. Konieczny, A. Prystupa, R.L. Castillo, E. Sze-Tu, Y. Xing, et al., Metabolic coordination between skin epithelium and type 17 immunity sustains chronic skin inflammation, Immunity 57 (2024) 1665–1680, https://doi.org/10.1016/j.immuni.2024.04.022, e1667.
[15] M.O.J. Grootaert, A. Finigan, N.L. Figg, A.K. Uryga, M.R. Bennett, SIRT6 protects smooth muscle cells from senescence and reduces atherosclerosis, Circ. Res. 128 (2021) 474–491, https://doi.org/10.1161/circresaha.120.318353.
[16] E. Verdin, NAD^+ in aging, metabolism, and neurodegeneration, Science 350 (2015) 1208–1213, https://doi.org/10.1126/science.aac4854.
[17] Q.J. Wu, T.N. Zhang, H.H. Chen, X.F. Yu, J.L. Lv, Y.Y. Liu, et al., The sirtuin family in health and disease, Signal Transduct. Targeted Ther. 7 (2022) 402, https://doi.org/10.1038/s41392-022-01257-8.
[18] J.E. Choi, C. Sebastian, C.M. Ferrer, C.A. Lewis, M. Sade-Feldman, T. LaSalle, et al., A unique subset of glycolytic tumour-propagating cells drives squamous cell carcinoma, Nat. Metab. 3 (2021) 182–195, https://doi.org/10.1038/s42255-021-00350-6.
[19] X. Wang, X. Zhao, X. Zheng, X. Peng, J. Chen, Y. Wang, et al., Sirt6 loss activates Got1 and facilitates cleft palate through abnormal activating glycolysis, Cell Death Dis. 16 (2025) 159, https://doi.org/10.1038/s41419-025-07465-8.
[20] H. Jiang, S. Khan, Y. Wang, G. Charron, B. He, C. Sebastian, et al., SIRT6 regulates TNF-α secretion through hydrolysis of long-chain fatty acyl lysine, Nature 496 (2013) 110–113, https://doi.org/10.1038/nature12038.
[21] M. Jedrusik-Bode, M. Studencka, C. Smolka, T. Baumann, H. Schmidt, J. Kampf, et al., The sirtuin SIRT6 regulates stress granule formation in C. elegans and mammals, J. Cell Sci. 126 (2013) 5166–5177, https://doi.org/10.1242/jcs.130708.
[22] K.Y. So, B.H. Park, S.H. Oh, Cytoplasmic sirtuin 6 translocation mediated by p62 polyubiquitination plays a critical role in cadmium-induced kidney toxicity, Cell Biol. Toxicol. 37 (2021) 193–207, https://doi.org/10.1007/s10565-020-09528-2.
[23] S. Luo, C. Kong, S. Zhao, X. Tang, Y. Wang, X. Zhou, et al., Endothelial HDAC1-ZEB2-NuRD complex drives aortic aneurysm and dissection through regulation of protein S-Sulfhydration, Circulation 147 (2023) 1382–1403, https://doi.org/10.1161/circulationaha.122.062743.
[24] H. Zhang, J. Pan, S. Huang, X. Chen, A.C.Y. Chang, C. Wang, et al., Hydrogen sulfide protects cardiomyocytes from doxorubicin-induced ferroptosis through the SLC7A11/GSH/GPx4 pathway by Keap1 S-sulfhydration and Nrf2 activation, Redox Biol. 70 (2024) 103066, https://doi.org/10.1016/j.redox.2024.103066.
[25] S. Fiorucci, E. Distrutti, Targeting the transsulfuration-H2S pathway by FXR and GPBAR1 ligands in the treatment of portal hypertension, Pharmacol. Res. 111 (2016) 749–756, https://doi.org/10.1016/j.phrs.2016.07.040.
[26] G.K. Kolluru, R.E. Shackelford, X. Shen, P. Dominic, C.G. Kevil, Sulfide regulation of cardiovascular function in health and disease, Nat. Rev. Cardiol. 20 (2023) 109–125, https://doi.org/10.1038/s41569-022-00741-6.
[27] N. Zhu, Z.F. Guo, K. Kazama, B. Yi, N. Tongmuang, H. Yao, et al., Epigenetic regulation of vascular smooth muscle cell phenotypic switch and neointimal formation by PRMT5, Cardiovasc. Res. 119 (2023) 2244–2255, https://doi.org/10.1093/cvr/cvad110.
[28] D. Torella, C. Iaconetti, R. Tarallo, F. Marino, G. Giurato, C. Veneziano, et al., miRNA regulation of the hyperproliferative phenotype of vascular smooth muscle cells in diabetes, Diabetes 67 (2018) 2554–2568, https://doi.org/10.2337/db17-1434.
[29] P. Luo, C. Qin, L. Zhu, C. Fang, Y. Zhang, H. Zhang, et al., Ubiquitin-specific peptidase 10 (USP10) inhibits hepatic steatosis, insulin resistance, and inflammation through Sirt6, Hepatology 68 (2018) 1786–1803, https://doi.org/10.1002/hep.30062.
[30] T. Hou, Y. Tian, Z. Cao, J. Zhang, T. Feng, W. Tao, et al., Cytoplasmic SIRT6-mediated ACSL5 deacetylation impedes nonalcoholic fatty liver disease by facilitating hepatic fatty acid oxidation, Mol. Cell 82 (2022) 4099–4115.e4099, https://doi.org/10.1016/j.molcel.2022.09.018.
[31] Y. Yang, L. Guo, L. Chen, B. Gong, D. Jia, Q. Sun, Nuclear transport proteins: structure, function, and disease relevance, Signal Transduct. Targeted Ther. 8 (2023) 425, https://doi.org/10.1038/s41392-023-01649-4.
[32] M.J. Morgan, Z.G. Liu, Crosstalk of reactive oxygen species and NF-κB signaling, Cell Res. 21 (2011) 103–115, https://doi.org/10.1038/cr.2010.178.
[33] C.Y. Hsieh, H.Y. Hsiao, W.Y. Wu, C.A. Liu, Y.C. Tsai, Y.J. Chao, et al., Regulation of shear-induced nuclear translocation of the Nrf2 transcription factor in endothelial cells, J. Biomed. Sci. 16 (2009) 12, https://doi.org/10.1186/1423-0127-16-12.
[34] D.C. Liemburg-Apers, P.H. Willems, W.J. Koopman, S. Grefte, Interactions between mitochondrial reactive oxygen species and cellular glucose metabolism, Arch. Toxicol. 89 (2015) 1209–1226, https://doi.org/10.1007/s00204-015-1520-y.
[35] A. Sun, Y. Wang, J. Liu, X. Yu, Y. Sun, F. Yang, et al., Exogenous H2S modulates mitochondrial fusion-fission to inhibit vascular smooth muscle cell proliferation in a hyperglycemic state, Cell Biosci. 6 (2016) 36, https://doi.org/10.1186/s13578-016-0102-x.
[36] L. Zhang, X. Jiang, N. Liu, M. Li, J. Kang, L. Chen, et al., Exogenous H(2) S prevents the nuclear translocation of PDC-E1 and inhibits vascular smooth muscle cell proliferation in the diabetic state, J. Cell Mol. Med. 25 (2021) 8201–8214, https://doi.org/10.1111/jcmm.16688.
[37] G. Cirino, C. Szabo, A. Papapetropoulos, Physiological roles of hydrogen sulfide in Mammalian cells, tissues, and organs, Physiol. Rev. 103 (2023) 31–276, https://doi.org/10.1152/physrev.00028.2021.
[38] S.I. Bibli, J. Hu, M. Looso, A. Weigert, C. Ratiu, J. Wittig, et al., Mapping the endothelial cell S-Sulfhydrome highlights the crucial role of Integrin sulfhydration in vascular function, Circulation 143 (2021) 935–948, https://doi.org/10.1161/circulationaha.120.051877.
[39] A.R. Chang, C.M. Ferrer, R. Mostoslavsky, SIRT6, a Mammalian deacylase with multitasking abilities, Physiol. Rev. 100 (2020) 145–169, https://doi.org/10.1152/physrev.00030.2018.
[40] X. Wu, H. Liu, A. Brooks, S. Xu, J. Luo, R. Steiner, et al., SIRT6 mitigates heart failure with preserved ejection fraction in diabetes, Circ. Res. 131 (2022) 926–943, https://doi.org/10.1161/circresaha.121.318988.
[41] K. Peng, C. Zeng, Y. Gao, B. Liu, L. Li, K. Xu, et al., Overexpressed SIRT6 ameliorates doxorubicin-induced cardiotoxicity and potentiates the therapeutic efficacy through metabolic remodeling, Acta Pharm. Sin. B 13 (2023) 2680–2700, https://doi.org/10.1016/j.apsb.2023.03.019.
[42] Y.N. Ding, T.T. Wang, S.J. Lv, X. Tang, Z.Y. Wei, F. Yao, et al., SIRT6 is an epigenetic repressor of thoracic aortic aneurysms via inhibiting inflammation and senescence, Signal Transduct. Targeted Ther. 8 (2023) 255, https://doi.org/10.1038/s41392-023-01456-x.
[43] W. Li, W. Feng, X. Su, D. Luo, Z. Li, Y. Zhou, et al., SIRT6 protects vascular smooth muscle cells from osteogenic transdifferentiation via Runx2 in chronic kidney disease, J. Clin. Investig. 132 (2022), https://doi.org/10.1172/jci150051.
[44] M. Aksu, S. Trakhanov, A. Vera Rodriguez, D. Görlich, Structural basis for the nuclear import and export functions of the biportin Pdr6/Kap122, J. Cell Biol. 218 (2019) 1839–1852, https://doi.org/10.1083/jcb.201812093.
[45] J. Xie, X. Long, L. Gao, S. Chen, K. Zhao, W. Li, et al., Respiratory syncytial virus nonstructural protein 1 blocks glucocorticoid receptor nuclear translocation by targeting IPO13 and May account for glucocorticoid insensitivity, J. Infect. Dis. 217 (2017) 35–46, https://doi.org/10.1093/infdis/jix445.
[46] K.A. Gajewska, H. Lescesen, M. Ramialison, K.M. Wagstaff, D.A. Jans, Nuclear transporter Importin-13 plays a key role in the oxidative stress transcriptional response, Nat. Commun. 12 (2021) 5904, https://doi.org/10.1038/s41467-021-26125-x.
[47] D. Sun, S. Chen, S. Li, N. Wang, S. Zhang, L. Xu, et al., Enhancement of glycolysis-dependent DNA repair regulated by FOXO1 knockdown via PFKFB3 attenuates hyperglycemia-induced endothelial oxidative stress injury, Redox Biol. 59 (2023) 102589, https://doi.org/10.1016/j.redox.2022.102589.
[48] D. Zhao, S.W. Zou, Y. Liu, X. Zhou, Y. Mo, P. Wang, et al., Lysine-5 acetylation negatively regulates lactate dehydrogenase A and is decreased in pancreatic cancer, Cancer Cell 23 (2013) 464–476, https://doi.org/10.1016/j.ccr.2013.02.005.
[49] J. Jin, L. Zhang, X. Li, W. Xu, S. Yang, J. Song, et al., Oxidative stress-CBP axis modulates MOB1 acetylation and activates the Hippo signaling pathway, Nucleic Acids Res. 50 (2022) 3817–3834, https://doi.org/10.1093/nar/gkac189.
[50] Z. Li, D.J. Polhemus, D.J. Lefer, Evolution of hydrogen sulfide therapeutics to treat cardiovascular disease, Circ. Res. 123 (2018) 590–600, https://doi.org/10.1161/circresaha.118.311134.
[51] H.J. Sun, Q.B. Lu, X.X. Zhu, Z.R. Ni, J.B. Su, X. Fu, et al., Pharmacology of hydrogen sulfide and its donors in cardiometabolic diseases, Pharmacol. Rev. 76 (2024) 846–895, https://doi.org/10.1124/pharmrev.123.000928.
[52] M. Wang, S. Zhang, J. Tian, F. Yang, H. Chen, S. Bai, et al., Impaired iron-sulfur cluster synthesis induces mitochondrial PARthanatos in diabetic cardiomyopathy, Adv. Sci. (Weinh.) 12 (2025) e2406695, https://doi.org/10.1002/advs.202406695.